Title

Ensemble-based deep learning for estimating PM2.5 over California with multisource big data including wildfire smoke

Authors

Li, Lianfa
Girguis, Mariam
Lurmann, Frederick
et al.

Publication Date

2020-12-01

DOI

10.1016/j.envint.2020.106143

Peer reviewed

HHS Public Access

Author manuscript

Environ Int. Author manuscript; available in PMC 2021 December 01.

Published in final edited form as:

Environ Int. 2020 December ; 145: 106143. doi:10.1016/j.envint.2020.106143.

Ensemble-Based Deep Learning for Estimating $PM_{2.5}$ over California with Multisource Big Data Including Wildfire Smoke

Lianfa Li[1,2,*], **Mariam Girguis**[1], **Frederick Lurmann**[3], **Nathan Pavlovic**[3], **Crystal McClure**[3], **Meredith Franklin**[1], **Jun Wu**[4], **Luke D. Oman**[5], **Carrie Breton**[1], **Frank Gilliland**[1], **Rima Habre**[1,*]

[1.]Department of Preventive Medicine, University of Southern California, Los Angeles, CA, USA

[2.]State Key Laboratory of Resources and Environmental Information System, Institute of Geographical Sciences and Natural Resources, Chinese Academy of Sciences, Beijing, China

[3.]Sonoma Technology, Inc., Petaluma, CA, USA

[4.]Program in Public Health, Susan and Henry Samueli College of Health Sciences, University of California, Irvine, CA, USA

[5.]Goddard Space Flight Center, National Aeronautics and Space Administration, Greenbelt, MD, USA

Abstract

Introduction: Estimating $PM_{2.5}$ concentrations and their prediction uncertainties at a high spatiotemporal resolution is important for air pollution health effect studies. This is particularly challenging for California, which has high variability in natural (e.g, wildfires, dust) and anthropogenic emissions, meteorology, topography (e.g. desert surfaces, mountains, snow cover) and land use.

[*]**Corresponding authors** Lianfa Li; Rima Habre, Division of Environmental Health, USC Keck School of Medicine, 2001 N. Soto Street, Suite 102, Los Angeles, CA 90089, Phone: +1 (323) 442-8283, lianfali@usc.edu (L. Li); habre@usc.edu (R. Habre).

Lianfa Li: Conceptualization, Methodology, Formal Analysis, Validation, Writing - Original Draft and Revising
Mariam Girguis: Investigation, Data curation
Frederick Lurmann: Conceptualization, Resource, Data curation, Writing - Review & Editing
Nathan Pavlovic: Resource, Data curation, Writing - Review & Editing
Crystal McClure: Resource, Data curation
Meredith Franklin: Conceptualization, Resource, Writing - Review & Editing
Jun Wu: Resources, Data curation, Writing - Review & Editing
Luke D. Oman: Resource, Data curation
Carrie Breton: Project administration, Writing - Review
Frank Gilliland: Project administration, Writing - Review
Rima Habre: Project administration, Investigation, Conceptualization, Writing - Review & Editing

Declaration of interests

The authors declare that they have no known competing financial interests or personal relationships that could have appeared to influence the work reported in this paper.

Appendix A. Supplementary data

Additional information regarding methods used, technical details, and results.

Methods: Using ensemble-based deep learning with big data fused from multiple sources we developed a $PM_{2.5}$ prediction model with uncertainty estimates at a high spatial (1km × 1km) and temporal (weekly) resolution for a 10-year time span (2008–2017). We leveraged autoencoder-based full residual deep networks to model complex nonlinear interrelationships among $PM_{2.5}$ emission, transport and dispersion factors and other influential features. These included remote sensing data (MAIAC aerosol optical depth (AOD), normalized difference vegetation index, impervious surface), MERRA-2 GMI Replay Simulation (M2GMI) output, wildfire smoke plume dispersion, meteorology, land cover, traffic, elevation, and spatiotemporal trends (geo-coordinates, temporal basis functions, time index). As one of the primary predictors of interest with substantial missing data in California related to bright surfaces, cloud cover and other known interferences, missing MAIAC AOD observations were imputed and adjusted for relative humidity and vertical distribution. Wildfire smoke contribution to $PM_{2.5}$ was also calculated through HYSPLIT dispersion modeling of smoke emissions derived from MODIS fire radiative power using the Fire Energetics and Emissions Research version 1.0 model.

Results: Ensemble deep learning to predict $PM_{2.5}$ achieved an overall mean training RMSE of 1.54 μg/m^3 (R^2: 0.94) and test RMSE of 2.29 μg/m^3 (R^2: 0.87). The top predictors included M2GMI carbon monoxide mixing ratio in the bottom layer, temporal basis functions, spatial location, air temperature, MAIAC AOD, and $PM_{2.5}$ sea salt mass concentration. In an independent test using three long-term AQS sites and one short-term non-AQS site, our model achieved a high correlation (>0.8) and a low RMSE (<3 μg/m^3). Statewide predictions indicated that our model can capture the spatial distribution and temporal peaks in wildfire-related $PM_{2.5}$. The coefficient of variation indicated highest uncertainty over deciduous and mixed forests and open water land covers.

Conclusion: Our method can be generalized to other regions, including those having a mix of major urban areas, deserts, intensive smoke events, snow cover and complex terrains, where $PM_{2.5}$ has previously been challenging to predict. Prediction uncertainty estimates can also inform further model development and measurement error evaluations in exposure and health studies.

Keywords

$PM_{2.5}$; machine learning; air pollution exposure; wildfires; remote sensing; California; high spatiotemporal resolution

1. Introduction

Exposure to fine particulate matter with aerodynamic diameter smaller than 2.5μm ($PM_{2.5}$) is associated with a range of acute and chronic adverse health effects (EPA 2017; WHO 2013a, b) including mortality (Atkinson et al. 2014) and morbidity (Lu et al. 2015). Studies have documented $PM_{2.5}$ effects on multiple organ systems and health outcomes including cardiovascular (Liang et al. 2014; Lippmann 2014), respiratory (Xing et al. 2016), atherosclerosis (Allen et al. 2012; Kunzli et al. 2010), birth outcomes (Yuan et al. 2019; Zhu et al. 2015), neurodevelopment and cognitive functions (Fu et al. 2019; Zheng et al. 2019). Accurate estimation of $PM_{2.5}$ exposures at a high spatiotemporal resolution is important for evaluating its health effects, particularly at small temporal (days to weeks) and spatial (neighborhood) scales. Although many countries have a substantial network of regulatory

$PM_{2.5}$ monitoring stations, their spatial coverage is still very limited in terms of accurately representing population exposures, especially in regions of the world that have complex spatiotemporal variability in emissions, topography, meteorology, land-use and population density, such as the state of California (CA) in the United States (US) (Lee 2019; Li et al. 2015; Liu et al. 2009; Monn 2001).

The Moderate Resolution Imaging Spectroradiometer (MODIS) instruments onboard the polar-orbiting TERRA and AQUA satellites, launched in in 2000 and 2002, respectively, provide daily aerosol optical depth (AOD) data which have been widely used to increase spatial coverage for estimating ground-level $PM_{2.5}$ concentrations. AOD is a column-integrated sum of total ambient particle extinction and is significantly correlated with ground/surface $PM_{2.5}$ (Toth et al. 2014). MODIS AOD products generated using the early Dark Target (DT) and Deep Blue (DB) algorithms (spatial resolution: 3–10 km), and the recent Multiangle Implementation of Atmospheric Correction (MAIAC) algorithm (spatial resolution: 1 km) have been used as reliable predictors of $PM_{2.5}$ concentrations (Chu et al. 2016). For example, the addition of satellite AOD improved the Pearson's correlation between estimated and observed $PM_{2.5}$ in the US by 0.3–0.6 (Chu et al. 2016; van Donkelaar et al. 2006) and over Massachusetts increased the model adjusted R^2 by 0.31 (Liu et al. 2009).

MODIS AOD can also provide information on wildfires (Ichoku and Ellison 2014), an increasingly important area of study in California due to their increasing frequency, environmental damage and associated health impacts, particularly in terms of exacerbations of asthma and chronic obstructive pulmonary disease (Reid et al. 2016). However, MODIS AOD retrievals are unreliable in the presence of thick smoke plumes as they can be misclassified as cloud (Ichoku and Ellison 2014; Livingston et al. 2014). Retrievals are also difficult over bright reflective surfaces such as deserts and in the presence of snow, cloud cover or glint. The MAIAC algorithm was developed to overcome some of these retrieval data quality issues (Lyapustin et al. 2011), yet in complex terrains such as California, issues remain. For example we found 41% of daily MAIAC AOD were missing over California during 2000–2016 (Li et al. 2020), which can have considerable impact on applications of satellite AOD in $PM_{2.5}$ estimation especially in the Western US (Chu et al. 2016). We recently developed a method using residual deep learning to reliably impute missing MAIAC AOD at a high spatial (1 km × 1 km) and temporal (weekly) resolution in California (Li et al. 2020) based on Modern-Era Retrospective analysis for Research and Applications Global Modeling Initiative Replay Simulation (M2GMI) AOD (Strode et al. 2019), meteorology, elevation and geographic coordinates with improved performance (mean test R^2 0.94; independent test R^2 with AErosol RObotic NETwork (AERONET) AOD: 0.69), compared with the existing imputation methods of MODIS AOD (Di et al. 2016; Kloog 2016; Lv et al. 2016; Xiao et al. 2017).

Early studies using satellite AOD to estimate $PM_{2.5}$ established the AOD-$PM_{2.5}$ relationship using empirical statistical correlation (Gupta et al. 2006; Kloog et al. 2011), two stage generalized additive models (Liu et al. 2009) and land-use regression (LUR) plus Bayesian maximum entropy (BME) (Beckerman et al. 2013) with cross validation (CV) R^2 of approximately 0.60–0.81 at a coarse spatial resolution (8.9–12 km). Later, mixed effects

models (Just et al. 2015; Lee et al. 2009; Lee et al. 2015; Xie et al. 2015) and geographically weighted regressions (GWR) (Bai et al. 2016; Guo et al. 2017; Hu et al. 2014) were widely used due to flexibility of allowing the AOD-$PM_{2.5}$ relationship to vary in space and/or time. Recently, machine learning (ML) methods including random forests (Brokamp et al. 2017; Huang et al. 2018; Wei et al. 2019), feed-forward neural network (Biancofiore et al. 2017; Di et al. 2016; Feng et al. 2015) and ensemble learning (Di et al. 2019; Li et al. 2018) have been increasingly used in estimation of $PM_{2.5}$ with improved performances (CV or test R^2 generally > 0.8). Although these existing methods achieved competent performance, compared with modern deep learning methods, LUR, generalized additive model (GAM) and mixed models have limitations in flexibility and learning capacity. Deep learning leverages multiple layers of artificial neural networks to progressively extract advanced features or representations from the model inputs. Due to the flexibility (unlimited hidden layers with their numbers of nodes) of network structure, a deep neural network has strong learning capacity to model non-linear associations and interactions among variables that can automatically extract advanced representations compared with many traditional ML algorithms, including GAM, support vector machine and Gaussian process regression (Goodfellow et al. 2016). Compared with random forests or other decision tree-based algorithms, deep neural networks do not require discretization of the input features, maintaining their full value ranges. Such discretization may lead to abrupt spatial variation in the predictions for the tree-based algorithms if limited training samples were used. On the other hand, the feed-forward neural network with deep hidden layers may have the issue of gradient vanishing during learning. Thus, residual learning may be employed to improve the learning (He et al. 2016a).

Although recent $PM_{2.5}$ modeling efforts that have incorporated satellite AOD data with other variables achieved a high CV R^2 of 0.80–0.86 (root mean square error (RMSE): 2.79–2.94 $\mu g/m^3$) for the contiguous US (Di et al. 2019; Di et al. 2016; Hu et al. 2017), considerable regional differences in model performance remain. Particularly, the southwestern or Pacific regions of US where CA is located had lower R^2 (0.74–0.80) and higher RMSE (2.85–4.05 $\mu g/m^3$) than national averages or eastern regions of US. In California, $PM_{2.5}$ concentrations are generally elevated in winter compared to summer due to high emissions of aerosol precursors, topography, and low mixing height (Toth et al. 2014; van Donkelaar et al. 2006). In winter, the surface $PM_{2.5}$-satellite relationship is further complicated by aerosol vertical distribution, high relative humidity (Li et al. 2015) and high cloud and snow cover leading to a greater proportion of missing data. Throughout the year, the impact of wildfire smoke also presents challenges to the use of satellite observations for prediction of ground-level $PM_{2.5}$ in CA. Satellite AOD retrievals over smoke plumes are masked as cloud and discarded in some AOD products. For locations where AOD retrievals are not masked, there is difficulty in representing the vertical distribution of the smoke, as smoke may be present aloft and detected by satellite while having no impact on surface pollution. Therefore, accurate estimation of ground-level $PM_{2.5}$ is particularly challenging for CA. Previous studies have overcome some challenges by omitting periods of high $PM_{2.5}$ (Larsen et al. 2020), which is likely to exclude peak $PM_{2.5}$ concentrations due to wildfire smoke. Given recent increases in wildfire event frequency (Dennison et al. 2014) and magnitude along with the substantial contribution of these events to enhanced $PM_{2.5}$ (Larsen et al. 2020; Larsen et al. 2018), there

is a need to ensure that $PM_{2.5}$ models used in exposure studies adequately represent wildfire smoke while also addressing the other challenges of air quality modeling that impact CA. In addition, there are no outputs of uncertainty for the estimated $PM_{2.5}$ in most existing studies using ML methods (Chu et al. 2016) even though such uncertainty can inform the user on areas for model improvement, confidence in and variability of $PM_{2.5}$ predictions, and can be used in downstream analyses of health effects to decrease the potential bias (Girguis et al. 2019, 2020).

In this study we developed an ensemble-based deep learning model to estimate $PM_{2.5}$ over CA by fusing multisource big data, including modeled dispersion of wildfire smoke. In ensemble learning, the autoencoder-based full residual deep network was used as a base model to model non-linear associations and complex interactions among the variables with the state-of-the-art performance, as demonstrated in our previous study (Li et al. 2020). In order to account for high variability of $PM_{2.5}$ in CA, we used the imputed MAIAC AOD with the full spatial coverage, MERRA-2 GMI Replay Simulation (M2GMI) data, land use data, traffic variables, and modeled wildfire smoke plume dispersion. Based on MERRA2, M2GMI improves the representation of transport and chemistry with higher spatial and temporal resolution, compared with previous MERRA-2 simulations (Strode et al. 2019). In addition, meteorological variables were extracted from the high-resolution gridMET dataset (e.g., air temperature, surface shortwave radiation, specific humidity, precipitation, wind speed) (Abatzoglou 2011) and the background-scale M2GMI (e.g., planetary boundary layer height (PBLH), wind speeds at different altitudes, evaporation land) (Brauer et al. 2016; Randles et al. 2017). Other remotely sensed data (normalized difference vegetation index (NDVI), impervious surface and land cover) were also used. Geo-coordinates, temporal basis functions and time index were used to capture spatiotemporal trends in $PM_{2.5}$ concentration. Using the big data from multiple sources in a parallel computing environment, we conducted preprocessing, downscaling of various parameters to the target spatial scale (1km × 1km) aggregating daily into weekly data, training of the models and outputting gridded $PM_{2.5}$ concentration and uncertainty estimates. By validation and comparison with $PM_{2.5}$ contributed by wildfires smoke, this study shows the importance of a robust deep learning method and sufficient features (including wildfire smoke plumes) to capture spatiotemporal variability of $PM_{2.5}$ for a large region with diverse aerosol emission sources, including wildfires, topography and meteorology. Our proposed method can be also applied to other similarly heterogeneous and complex regions.

Supplementary Table S1 provides a list and brief description of all acronyms used in this paper.

2. Materials

2.1. Study Domain

Our study domain (Fig. 1) is the state of California located between approximately −124°65’ and −114°13’ west to east longitude and between 32°51’ to 42°01’ north to south latitude. With an area of 423,970 km^2, CA has heterogenous topography (desert surfaces, mountains, snow cover), aerosol emission sources (e.g., natural sources: wildfires and dust; anthropogenic sources: fossil fuel exhaust, agriculture, and biomass burning) and

meteorological processes (Fast et al. 2014). This subsequently results in differences in AOD (more reflective surfaces), the chemical composition of $PM_{2.5}$ (more contribution of nitrate (Tolocka et al. 2001)) and seasonal variation in aerosol vertical distribution, compared to eastern states of the US (Fast et al. 2014; Li et al. 2015).

2.2. $PM_{2.5}$ Measurements

We obtained daily $PM_{2.5}$ measurements (2008–2017) from the United States Environmental Protection Agency (EPA) Air Quality System (AQS) (https://www.epa.gov/aqs) that were collected by state, local, and tribal air pollution control agencies. We also obtained spatially dense (267 locations) biweekly $PM_{2.5}$ samples (2008–2009) from the University of Southern California Intra-Community Variability study 2 (ICV2). These samples were collected in 8 southern California communities from Santa Barbara south to Riverside (Figure 1) using Harvard Cascade Impactors described in more detail in (Fruin et al. 2014). To temporally downscale biweekly ICV2 samples to weekly values, we derived a scaling ratio of weekly to biweekly means based on the AQS stations closest to the ICV sites. We chose to develop a $PM_{2.5}$ model with weekly temporal resolution because this was the shortest exposure window needed for anticipated epidemiologic analyses of pregnancy outcomes. The AQS $PM_{2.5}$ network includes both continuous monitoring and 24-hour sampling on a 1-in-6 day, 1-in-3 day and everyday schedule. The 2008–2017 database provides daily $PM_{2.5}$ measurements for about half of days at the sites that measured $PM_{2.5}$ for at least one year. Measurements alone would provide only 43% valid weekly values using EPA's 75% completeness criteria at these sites. Linear regression models were developed to fill in missing daily values at most sites by using daily data from nearby sites (within 50 km) with significant data availability (more than 1 year of data). The median R^2 was 0.74 (IQR=0.63 to 0.83) for all regression models; two-thirds of daily estimates were made using "two-nearby sites" regression models (median R^2=0.77). Weekly values for model training and evaluation were developed using at least 5 daily measurements (allowing up to maximum of 2 daily values estimated from the regression models). The fill in procedures increase the availability of complete weekly samples from 43% to 79% in the 2008–2017 period, with a trend of increasing completeness in the later years because of increased deployment of continuous monitors.

For weekly $PM_{2.5}$ predictions we generated a fixed spatial grid of 1 km × 1 km over California using the Universal Transverse Mercator (UTM) zone 11N coordinate system (ellipsoid: World Geodetic System 1984, unit: meter).

2.3. Features

2.3.1 MAIAC AOD—As an advanced algorithm, MAIAC leverages a spatial and temporal algorithm to simultaneously retrieve atmospheric aerosols and bidirectional reflectance from MODIS data. Compared with the DT and DB algorithms, MAIAC further detects clouds and corrects atmospheric effects over both dark vegetated surfaces and bright desert targets to obtain better daily AOD values at a higher spatial resolution (1 km × 1 km) (Lyapustin et al. 2018). The algorithm is also tuned to reduce masking of wildfire smoke as clouds (Lyapustin et al. 2012). We acquired MAIAC AOD (at 550 nm with quality assurance flags) covering California for 9 years (01/01/2008 to 12/31/2016) from MODIS TERRA and AQUA

satellites that had equatorial crossing at about 10:30 AM and 1:30 PM local time, respectively, from a NASA ftp site (ftp://maiac@dataportal.nccs.nasa.gov/DataRelease; the website is inaccessible now). We obtained 2017 MAIAC AOD from the updated NASA website (https://lpdaac.usgs.gov/products/mcd19a2v006/) which had a change in the projection used from Alberts to the global Sinusoidal projection. Therefore, all the MAIAC AOD images were converted into the target projection of UTM Zone 11. The evaluation with AERONET measurements using co-located samples (Supplementary Table S2) showed consistency in MAIAC AOD between 2008–2016 and 2017 with a very small difference (Pearson's correlation>0.91 with $p\text{-}value<0.01$). We used autoencoder-based residual deep network to impute missing MAIAC AOD with a high performance as described in our earlier work (Li et al. 2020).

2.3.2 Meteorology—Meteorological factors play very important roles in forming, dispersion and transport of $PM_{2.5}$ at regional and local scales (Chu et al. 2016). We extracted meteorological parameters from daily high spatial resolution (~4 km, 1/24th degree) surface meteorological data for the gridMET of the contiguous US (http://www.climatologylab.org/gridmet.html) (Abatzoglou 2011). These parameters include daily minimum air temperature (°C), maximum air temperature (°C), wind speed (meters/second, m/s), specific humidity (grams of vapor per kilogram of air, g/kg), daily mean downward shortwave radiation (watt/meter^2, w/m^2) and accumulated precipitation (millimeters of rain per meter^2 in 1 h, mm/m^2). Weekly averages of the meteorological features were generated from daily values. Bilinear resampling was used to transform the meteorological data into the target UTM Zone 11 projection.

2.3.3 MERRA-2 Global Modeling Initiative Replay Simulation—The MERRA-2 Global Modeling Initiative output (publicly available from https://portal.nccs.nasa.gov/datashare/merra2_gmi) is generated through the simulation for the atmospheric composition coupling MERRA2 meteorological fields (winds, temperature and pressure) with the Global Modeling Initiative (GMI)'s stratosphere-troposphere chemical mechanism. The simulation is interactively coupled to the Goddard Chemistry Aerosol Radiation and Transport module and includes similar emissions to what was used for MERRA-2 (NASA 2018; Strode et al. 2019). From M2GMI bottom layer, we extracted 30 modeled gaseous air pollutants and particulate matter source contributions in the $PM_{2.5}$ size fraction (including carbon monoxide, nitrogen dioxide and oxide, ozone, and mass concentrations of sea salt, nitrate, sulfur dioxide, ammonia, sulfate, organic carbon, dust, and black carbon), 12 meteorological parameters (including PBLH, air temperature, specific humidity, precipitation, wind speed) and 24 other parameters at ~50km spatial resolution. From 66 M2GMI variables, we selected 18 as predictors based either on their correlations (absolute value >= 0.05) with weekly $PM_{2.5}$ concentration or plausible physical interpretation for their influence on $PM_{2.5}$ concentrations. Based on M2GMI wind speeds at 10 m and 50 m altitudes, we derived indicators of vertical stagnation and wind sheer/mechanical mixing as follows:

$$w_{\text{stag}} = \left(\sqrt{u_{50}^2 + v_{50}^2} - \sqrt{u_{10}^2 + v_{10}^2}\right) \quad (1)$$

$$w_{\text{mix}} = \left(\sqrt{u_{10}^2 + v_{10}^2} - \sqrt{u_2^2 + v_2^2}\right) \quad (2)$$

where w_{stag} is the indicator of stagnation, w_{mix} is wind sheer/mechanical mixing, u_{10} is 10-meter eastward wind speed, v_{10} is 10-meter northward wind speed, u_2 is 2-meter eastward wind speed, v_2 is 2-meter northward wind speed, u_{10} is 50-meter eastward wind speed, and v_{50} is 50-meter northward wind speed.

2.3.4 Wildfire Smoke Plume Dispersion Modeling—Wildfire smoke plumes can result in peak $PM_{2.5}$ concentrations and considerably affect spatiotemporal variability of $PM_{2.5}$ in California. We calculated ground-level $PM_{2.5}$ from smoke using dispersion modeling of primary emissions of $PM_{2.5}$ from wildfires, where emissions were determined from the Fire Energetics and Emissions Research version 1.0 (FEER.v1) model (Ichoku and Ellison 2014) with MODIS Aqua and Terra fire radiative power retrievals. To capture local impacts and long-range smoke transport, we estimated emissions from all fires in California and all large fires (>1000 acres) throughout the western U.S. and portions of Canada and Mexico. Fire area was calculated using ecoregion-specific per-detect area estimates, as in the 2014 National Emissions Inventory (EPA 2018). To reduce computational requirements, we clustered all hotspots within 0.05° using the density-based DBSCAN methodology (Ester et al. 1996) and summed the emissions of clustered hotspots.

We modeled smoke dispersion using the Hybrid Single-Particle Lagrangian Integrated Trajectory (HYSPLIT) model (Stein et al. 2015) and calculated smoke injection height using the Sofiev et al. (2013) model. We distributed daily emissions totals using the hourly emissions profile using the WRAP time profile (Western Regional Air Partnership 2005), which estimates minimal emissions (<0.01%) between 8 PM and 9 AM, with peak emissions at 4 PM (17% of total emissions). Dispersion was driven using North American Mesoscale Forecasting System (NAM) 12 km gridded meteorological data, which was obtained from NOAA Air Resources Laboratory (https://www.ready.noaa.gov/archives.php). $PM_{2.5}$ from smoke was carried over for up to 5 days from smoke release. The HYSPLIT model's 100m surface layer concentrations were used as ground-level $PM_{2.5}$ from smoke. We estimated resulting concentrations on the NAM 12km grid on an hourly time step. To prepare the data for subsequent modeling, we averaged the hourly data to weekly concentrations and further downscaled the weekly values from 12-km to 1-km resolution using bilinear interpolation.

2.3.5 Land Cover Variables—Land use parameters can capture $PM_{2.5}$ emission sources and sinks and have been used in many studies. The National Land Cover Database (NLCD) (https://www.mrlc.gov) provides nationwide data on land cover and its change at a 30m resolution. From the NLCD, we generated annual percent cover of each land cover class on the target modeling grid of 1 km (Yang et al. 2018). For each of 16 land cover classes (e.g., open water, developed with low intensity, developed with high intensity, barren land, grassland and cultivated crops etc.), we calculated the proportion of cover between 0 and 1 of each class within 1km grid cells for each available year (2001, 2003, 2006, 2008, 2011, 2013, and 2016), and linearly interpolated to annual values for unavailable years of

2001–2016. We used 2016 land cover data for 2017. For the $PM_{2.5}$ modeling, we excluded the land cover types that were not as frequently observed in CA (<1%).

From the NLCD, we also extracted the surface imperviousness layer that represents urban impervious surfaces as a percentage of developed surface over every 30-meter pixel in the US for the years 2001, 2006, 2011, and 2016. We used similar linear interpolation to derive impervious surface percentage in missing years (also assuming no change for 2017).

We calculated monthly average NDVI using 16-day MODIS NDVI average values from NASA's Aqua and Terra satellite (MOD13A2 V6 and MCD13A2 V6). The 16-day NDVI product was obtained on a 1km resolution grid, and we resampled the final monthly averages to the standard 1 km modeling grid described above.

2.3.6 Temporal Basis Functions—Using iterative singular value decomposition, we extracted four temporal basis functions (Finkenstadt et al. 2007) from the AQS $PM_{2.5}$ measurements of 10 years (2008–2017). As shown in our previous study (Li et al. 2019), four temporal basis functions represented the major temporal trend of $PM_{2.5}$ concentrations from 2008 to 2017 for CA, and can be used in the models to capture long- and short-term temporal variability of $PM_{2.5}$ over a complex and large region like CA.

2.3.7 Elevation, Geographic Coordinates and Time Index—We obtained 30 m resolution elevation from GoogleMaps API and calculated its average within each 1 km MAIAC grid cell. The central x and y coordinates of the target resolution of 1×1 km^2 with the target projection were used to account for spatial variability. The day of year was used to account for seasonal variability and the year index was used to account for annual variability.

3. Methods

In order to model the non-linear associations and complex interactions among the features and $PM_{2.5}$ concentration, an autoencoder-based full residual deep network was used in three phases: downscaling, imputation of missing AOD, and base model and ensemble learning.

Fig. 2 shows the flowchart of our $PM_{2.5}$ modeling process in California. The model inputs include multisource heterogeneous data (Fig. 2-a). From one input (M2GMI variables) we derived vertical stagnation and wind sheer, and from the $PM_{2.5}$ measurements we extracted four temporal basis functions (Sections 2.2-2.3). In order to have all regressors with the same projection and spatiotemporal resolution (1 km), preprocessing including resampling or downscaling, and imputation was performed for M2GMI variables and MAIAC AOD (Fig. 2-b, Section 3.1). Data cleaning, outlier filtering, AOD conversion and feature selection were also performed in preprocessing. With all data prepared, 100 residual deep network models were trained and validated (Section 3.2), ensemble predictions were made (Section 3.3) and evaluated (Section 3.4), and feature importance quantification and model interpretation were conducted (Section 3.5) (Fig. 2-c). After the optimal models were obtained, 1 km resolution gridded daily surfaces of $PM_{2.5}$ estimates with complete

spatiotemporal coverage over California were generated (Fig. 2-d; Section 4.4 for the results).

3.1. Preprocessing

Preprocessing includes data cleaning, removal of outliers, downscaling, imputing missing AOD, conversion of column MAIAC AOD to ground aerosol extinction coefficient, normalization and feature selection. In data cleaning, data quality flags (e.g., valid value range: (0, 3) for MAIAC AOD; (−1, 1) for NDVI; (0, 1) for land-use area proportion) were used to remove invalid values among each feature. The outer fence (NIST/SEMATECH 2016) was used to filter outliers. The downscaling algorithm based on residual deep network (Li et al. 2020) was used to downscale M2GMI variables (~50km spatial resolution) to the target resolution (1 km). In our downscaling, spatial coordinates, elevation and gridMET variables were used as the features at the target resolution. In addition, missing MAIAC AODs were imputed using residual deep network (Li et al. 2020). Normalization by standardization was performed to ensure all the variables to be on a consistent scale, and to stabilize model training (Bhandari 2020). For feature selection, the features with a low, non-statistically significant correlation (absolute value <0.02) with weekly $PM_{2.5}$ concentrations were removed from the list of potential predictors. Physical interpretability and redundancy were then considered to filter out remaining features. For example, M2GMI variables in the $PM_{2.5}$ size fraction or in the bottom surface layer were retained. M2GMI gases or other parameters were retained based on a priori knowledge of their physical or chemical relationship to $PM_{2.5}$ formation or dispersion, or interpretability.

In addition, an empirical formula was used to convert satellite column AOD to surface aerosol extinction coefficient (Wang et al. 2010) adjusting for vertical distribution and effects of relative humidity as follows:

$$k_g = \frac{\tau_c \cdot (1 - h/100)^g}{H_A} \tag{3}$$

where k_g is the converted surface-level aerosol extinction coefficient hypothesized to correlate more closely with ground measured $PM_{2.5}$ than column AOD, τ_c is column satellite AOD (MAIAC AOD), H_A is the scale height of aerosol, approximated by M2GMI PBLH (Koelemeijer et al. 2006), h is relative humidity (unit:%), and g is the empirical parameter to be optimized.

3.2. Base Model of Full Residual Deep Network

Full residual deep network was developed as the base model, which consists of the encoding layers (including the input layer and hidden layers with a decreasing number of nodes), the latent (coding) representation layer, the decoding layers, and the output layer (Fig. 3-a) (Li et al. 2020). In the autoencoder, the coding/latent layer is used to extract the representation from the input; each decoding layer has the same number of nodes corresponding to its symmetrical encoding layer. The latent layer has a compressed dimension to have a powerful representation for the input layer and help with efficient model training. Full residual connections in the autoencoder were introduced: each of the encoding layers has a shortcut

of identity mapping (residual connection) to its corresponding decoding layer to improve training and error back-propagation. Residual learning is an efficient method to appropriately increase the depth of the hidden layers without reduction in the performance. Inspired by the pyramidal cells in the cerebral cortex (Thomson 2010), residual learning utilizes shortcuts to jump over some layers, and thus reuse activations from a previous layer to reduce or avoid the problem of vanishing gradients (He et al. 2016b). Based on the encoding-decoding structure of autoencoder, full residual connections for all encoding layers and their corresponding decoding layers can be constructed in a nested way (Fig. 3-a) to considerably boost robustness in training and improve the generalization of the trained models, as demonstrated in our previous study (Li et al. 2020).

Given powerful capability to model the non-linear associations among the predictive features and the target variables, full residual deep network was used in three phases of this study: downscaling in preprocessing (Fig. 3-b), imputation of massive missing MAIAC AOD, and spatiotemporal estimation of $PM_{2.5}$ concentrations. Our previous study (Li et al. 2020) describes the downscaling algorithm in detail (also used to downscale the M2GMI variables in this study) and imputation of missing MAIAC AOD of 2000–2016 over CA (validation with AERONET AOD: correlation = 0.83; $R^2 = 0.69$). The same method was also used to impute missing MAIAC AOD of 2017 over CA.

For the output layer of $PM_{2.5}$ spatiotemporal estimation, we used the following loss function of a single output (estimate of $PM_{2.5}$ concentration):

$$\ell(\theta_{\mathrm{w,b}}) = \ell_{\mathrm{y}}\left(\mathbf{y}, f^{\mathrm{y}}_{\theta_{\mathrm{W,b}}}(\mathbf{X})\right) + \Omega(\theta_{\mathrm{w,b}}) \tag{4}$$

where $\ell_{\mathbf{y}}$ is the loss function of $PM_{2.5}$ without regularization, $\ell(\theta_{\mathbf{W,b}})$ is the final loss function with regularizer, **W** is the weight matrix, **b** is bias vector, $\theta_{\mathbf{W,b}}$ are the parameters for **W** and **b**, **y** is the ground truth of the target variable ($PM_{2.5}$ concentration), $f^{\mathrm{y}}_{\theta_{\mathrm{W,b}}}(\mathbf{X})$ is the estimate of **y** by the trained model for the input matrix **X**, $\Omega(\theta_{\mathbf{W,b}})$ is the regularizer of elastic net (Zou and Hastie 2005) that is defined as:

$$\Omega(\theta_{\mathbf{w,b}}) = \lambda_1 \left| \sum_{p \in \theta_{\mathrm{w,b}}} p \right| + \lambda_2 \sum_{p \in \theta_{\mathrm{w,b}}} p^2 \tag{5}$$

where $|\cdot|$ is the absolute value operator, p is the parameter to be learned within $\theta_{\mathbf{W,b}}$, λ_1 and λ_2 are the weights assigned as the hyper-parameters for lasso and ridge regularizers. Their optimal solution can be retrieved using grid search (Chicco 2017).

Due to the relatively small sample size of the $PM_{2.5}$ dataset in comparison with the satellite AOD dataset, the output of single parameter has a lower training bias and a better test performance than that of multiple parameters used in imputation of the MAIAC AOD (Li et al. 2020). An optimal network structure (the number of encoding layers and the number of nodes for each layer) was obtained using grid search.

3.3. Bagging and Ensemble Predictions

Using the full residual deep network as the base model, bootstrap aggregating (bagging) was conducted to obtain ensemble predictions (Fig. 3-c). Bootstrap sampling was conducted for the data samples and partially for the features. By bootstrap, we used approximately 63.3% of the samples for training and the remaining 36.7% of the samples for testing. In total, we had 59 predictive features available for modeling. Of these features, 28 had statistically significant correlation (absolute value >0.1) with $PM_{2.5}$ and were used as fixed predictors to keep the performance of the trained model above a certain level, and the remaining 31 features were sampled with replacement (see Supplementary Table S3). On average, approximately 50 predictive features in total were used in a base model. The ensemble predictions were obtained using the weighted averages of all the predictions of all the trained base models:

$$\hat{x}_w = \frac{\sum_{i=1}^{N} w_i \hat{x}_i}{\sum_{i=1}^{n} w_i} \tag{6}$$

$$\hat{\sigma}(\hat{x}_w) = \sqrt{\frac{\sum_{i=1}^{N} w_i (\hat{x}_i - \hat{x}_w)^2}{\frac{(N' - 1)\sum_{i=1}^{N} w_i}{N'}}} \tag{7}$$

where w_i is the weight assigned to model i (e.g., w_i=1/RMSE$_i$ in our study), $\hat{x}$ is the weighed sum, N is the number of samples, N' is the number of non-zero weights, $\hat{x}_w$ is the ensemble weighted estimate and $\hat{\sigma}(\hat{x}_w)$ is the estimate of standard deviation as an uncertainty metric for $\hat{x}_w$. From the estimated standard deviation, we derived the coefficient of variation through normalization by the predicted mean.

The bootstrap for the samples and the features was used to reduce the correlations among the trained models. In addition, we also introduced a small variation by sampling in a small interval ([−10, 10]) for the number of nodes for each hidden layer based on the optimal base model to reduce the correlation between the trained models. Theoretically, ensemble predictions with less standard error can be obtained by aggregating the outputs of the less correlated models. Assuming that ε_i is the error contained in each model's predictions with the errors drawn from a zero-mean multivariate normal distribution ($\mathbb{E}[\varepsilon^2] = v$ and $\mathbb{E}[\varepsilon_i \varepsilon_j]_{i \neq j} = c$), the expected squared error of the ensemble predictor is:

$$\mathbb{E}\left[\left(\frac{1}{m}\Sigma_i \varepsilon_i\right)^2\right] = \frac{1}{m^2}\mathbb{E}\left[\sum_i \left(\varepsilon_i^2 + \sum_{j \neq i} \varepsilon_i \varepsilon_j\right)\right] = \frac{v}{m} + \frac{(m-1)c}{m} \tag{8}$$

where m is the number of models, c represents the correlation in the errors between different models. If c=0 (no correlation), the squared error is just $\frac{1}{m}v$, indicating a linear decrease with the ensemble size. But if c=v (perfectly correlated, Pearson's correlation=1), the ensemble error does not change (still v). Thus, the smaller the Pearson's correlation, the smaller are the expected squared errors in the ensemble predictions.

In ensemble learning, we have several hyper-parameters, $\vartheta(m,\lambda_1,\lambda_2,l_r,n_b)$ (m: the number of trained models; λ_1 and λ_2: the weight for lasso and ridge regularizers; l_r: initial learning rate; n_b: the sample size of a mini batch in training) to be solved. In our method, due to the high learning efficiency the mini-batch gradient descent was used to find an optimal solution. In this optimization the training samples are split into small batches, where each batch of samples is iteratively used to calculate model error and update model coefficients. The sample size (n_b) of a mini batch is one of the important hyper-parameters for model training (Goodfellow et al. 2016). We used grid search to find an optimal solution for these parameters. We used the Spark big data platform for parallel data processing, ensemble training and grid search.

Another advantage of using ensemble learning to predict $PM_{2.5}$ is that we can derive the coefficient of variation for the predicted $PM_{2.5}$ as an uncertainty metric to inform the confidence degree of the predicted values.

In order to reduce the dependence between samples in each bootstrap, we used an effective stratification strategy. In this strategy, the samples were first divided into different groups based on the spatiotemporal factor of county id and month index; random shuffling and bootstrap were then conducted between different strata, and within each selected stratum. By merging all of the selected samples, we obtained the training samples for each bootstrap (the rest of the samples were used as the validation and test samples). As an improved version of non-overlapping simple block bootstrap that is generally used to bootstrap the samples in the time series data (Carlstein 1986), our method performed additional bootstrap sampling within each stratum. With the spatiotemporal stratification based on both county and month index, each stratum corresponded to a block, and the stratification method substantially reduced spatiotemporal dependence between blocks (strata). Compared with the original data, we obtained the training samples with less dependence between them. Sensitivity analyses were conducted to compare our stratification strategy and simple block bootstrap. In the simple block bootstrap, we first used K-Means to group the samples based on the coordinates and time index (week index) into 500 clusters (similar to the number of strata in our strategy), and then performed bootstrap at the block level and retrained the models.

3.4. Validation and Independent Test

By bootstrap between strata and within each stratum, we selected approximately 63.3% of the samples for training and validation, and the remaining 36.7% for independent test. Of the selected 63.3% of the samples, 80% were used in training and the remaining 20% were used in validation. The 36.7% of the total samples were used as the independent test.

In addition, we collected the time-series of $PM_{2.5}$ measurements from four monitoring sites for independent tests (Fig. 1). Data from three AQS routine sites were used for site-based independent testing (i.e., excluded from model training and validation). The three AQS sites were selected to represent northern, eastern and central populated sub-regions of CA (compared the less populated western sub-region). For the southern sub-region, we used data from the University of Southern California (USC) Particle Instrumentation Unit monitoring site in Los Angeles (Shirmohammadi et al. 2016) as a third-party independent test. This data was collected as part of a fine particle characterization study described in more detail in

Shirmohammadi et al. (2016) and was not used in model training and validation. Briefly, the USC site is located about 3 km south of downtown Los Angeles, CA. Five-day integrated samples were collected every week from Monday to Friday, between July 2012 and February 2013, using Micro-Orifice Deposit Impactors (MOUDIs, Model 110 MSP Corporation). Collocated AQS data at three other nearby sites from the same study were used in a generalized additive model to adjust the bias in the $PM_{2.5}$ measurements caused by the different instruments at the AQS sites and the USC monitoring site.

3.5. Feature Importance and Model Interpretation

In order to interpret the influence of key features in the trained models on performance, we used the Shapley Additive exPlanations (SHAP) tool (Lundberg and Lee 2017) to measure each predictor's average contribution (feature significance) to our trained model. In addition, we used the individual conditional expectation (ICE) plot (Goldstein et al. 2015) with partial dependence plot (PDP) (Friedman 2001) to visualize the relationship between each predictive feature and the target variable ($PM_{2.5}$ concentration). The PDP shows the marginal effect of one feature on the outcome of a trained model, and it can show whether the relationship between the target and a feature is linear, monotonic or more complex (non-linear). ICE plots can visualize the dependence of the prediction on a feature for each instance separately, resulting in one dependence line per instance, compared to one line overall in PDP.

4. Results

4.1. Summary and Correlation

In total, we included 34,812 weekly $PM_{2.5}$ samples among which, 34,005 routine samples were from 133 AQS sites, and 807 field samples were from 267 ICV2 locations (Fig. 1). The mean $PM_{2.5}$ concentration over the study region was 10.41 $\mu g/m^3$ (standard deviation: 6.21 $\mu g/m^3$) with higher values in winter than in summer (12.05 vs. 10.26 $\mu g/m^3$) and higher values in southern California than in northern California (10.95 vs. 9.49 $\mu g/m^3$) (Supplementary Fig. S1 for the boxplots and histograms of observed $PM_{2.5}$ and MAIAC AOD). Unlike the eastern US, California has a seasonal variation of higher AOD in summer than in winter (0.10 vs. 0.06), opposite to that of $PM_{2.5}$. Using Eq. (3) to convert MAIAC AOD to surface aerosol extinction coefficient with empirical parameter g=0.21, the correlation of MAIAC AOD with $PM_{2.5}$ improved from 0.25 to 0.47.

In total, we had 59 predictive features (MAIAC AOD, 20 M2GMI variables, 16 land-use variables, 6 meteorological variables, wildfire smoke, 2 traffic variables, 5 coordinates, NDVI, elevation, year, day of year, 4 temporal basis functions) and selected about 50 features for modeling in each bootstrap. The first 4 temporal basis functions were extracted from 133 AQS routine stations (Supplementary Fig. S2). Table 1 shows descriptive statistics for the feature in each category with an absolute correlation>0.1 with weekly $PM_{2.5}$ and Supplementary Fig. S3 shows the bar plot for the correlation of these selected features.

4.2. Optimal Base Model and Ensemble Learning

Through grid search we obtained an optimal benchmark structure with the encoding and latent layers having the numbers ([50, 128, 64, 32, 16]) of nodes for $PM_{2.5}$ estimation. Correspondingly, we had eleven layers in total with one input layer, four encoding layers, one latent layer, four decoding layers, and one output layer. For the hyper-parameters $\vartheta(m,\lambda_1,\lambda_2,l_r,n_b)$ in our optimal solution, we obtained an optimal number (m=100) of trained models, an initial learning rate (l_r=0.01), weights for elastic net (λ_1=0.5 and λ_2=0.5), and a mini batch size (n_b=512). In total, we trained 100 base models with each having a change in the number of nodes for each hidden layer based on the benchmark network structure. In summary (Table 2), we obtained mean training R^2 of 0.94 (range: 0.77 to 0.97) (mean training RMSE: 1.54 μg/m^3, range: 1.03–3.02 μg/m^3), and mean testing R^2 of 0.82 (range: 0.70 to 0.85) (mean testing RMSE: 2.70 μg/m^3, range: 2.46–3.49 μg/m^3) (Fig. 4).

Sensitivity analysis (Table 2 vs. Supplementary Table S4; Fig. 4 vs. Supplementary Fig. S4) showed better performance (mean test R^2: 0.82 vs. 0.72; by an improvement of 10%) for our stratified sampling, compared with simple block bootstrap. For ensemble predictions (Supplementary Fig. S5) of simple block bootstrap, we obtained test R^2 of 0.79, compared with the test R^2 of 0.87 in our stratification method (an improvement of 8%).

The ICE and PDP results (Supplementary Fig. S6-S7) illustrate marginal associations or/and interactions of MAIAC AOD, carbon monoxide, wildfire smoke, black carbon surface mass concentration, coordinates, wind speed, and air temperature etc. with $PM_{2.5}$. Plots are shown here for a single model (Model 1) and selected features that generally ranked among the highest predictive features across all 100 models.

For each single base model, we ranked the contribution of each predictor by calculating its SHAP value (Fig. 5-a for the top 20 features and Supplementary Fig. S8 for all the features). SHAP contributions were averaged over the 100 trained models (Fig. 5-b for the top 20 features and Supplementary Fig. S9 for all the features). As shown in these figures, the top 10 features across the 100 trained models included carbon monoxide, temporal basis function, coordinates (latitude, longitude, and their products), maximum temperature, MAIAC AOD, pressure, and sea salt surface $PM_{2.5}$.

4.3 Evaluation

In ensemble learning, the ensemble predictions by 100 trained models had an improvement of approximately 5% over the average performance of the single base model based on the test R^2 (0.87 vs. 0.82) (RMSE: 2.29 vs. 2.70 μg/m^3) (Table 3). Increasing the number of models beyond 100 only improved model performance very slightly, but added training time substantially. Compared with a single base model, the ensemble predictions had few extreme values and outliers (Fig. 6 for the scatter plots of observed vs. predicted (a) or residual (b) $PM_{2.5}$). The observed $PM_{2.5}$ and ensemble predicted $PM_{2.5}$ also presented very similar distributions (Supplementary Fig. S10 and S11 for their histograms and boxplots). The residuals of the ensemble predictions presented a normal distribution with mean close to zero and a small standard deviation (Supplementary Fig. S12). The autocorrelation was very low (mostly <0.08) between the residuals for most of lags (Supplementary Fig. S13),

indicating that spatiotemporal variability of $PM_{2.5}$ in this study region was well captured by our models.

The times series of predicted $PM_{2.5}$ for four sites (three routine AQS site and one USC site) in the independent test were shown in Fig. 7, and their R^2 and RMSE were shown in Table 4 (their locations shown in a, b, c and d of Fig. 1). The results show that the temporal (seasonal and yearly) trends and variations were well captured in the ensemble models (R^2: 0.67–0.87; RMSE: 1.80–2.81 μg/m^3).

4.4 Surfaces of Predicted $PM_{2.5}$ and Wildfires

The 1×1 km^2 surfaces of weekly $PM_{2.5}$ averages of ensemble predictions and their uncertainty (coefficient of variation) from 2008 to 2017 were generated based on bagging of the 100 trained models. The surfaces of four weeks in different seasons from 2008 to 2017 were shown in Fig. 8 (a and b: a spring week of April 21–27, 2008; c and d: a summer week of July 16–22, 2012; e and f: an autumn week of September 14–20, 2015; g and h: a winter week of December 25–31, 2017). The predicted surfaces show reasonable variation of $PM_{2.5}$ concentration across different seasons and across CA. The coefficient of variation (Fig. 8 –b, d, f, and h) showed higher uncertainty (mean: 0.57, standard deviation: 0.39) over deciduous forest, mixed forest and water bodies (e.g., lakes) (Supplementary Fig. S14) or high altitude. This might be indirectly caused by false high AOD due to water, snow in winter (higher uncertainty in winter than in summer), cloud or other high reflectance. These uncertainty estimates provide a quantitative estimate of variability or confidence in predicted $PM_{2.5}$ and can be incorporated into analyses examining measurement error in these predictions and its subsequent impact on health effect estimates in downstream (Girguis et al. 2019, 2020).

Historically wildfires in CA most frequently occur in summer and autumn. Fig. 8- c and e presents predicted surfaces of $PM_{2.5}$ for two weeks impacted by wildfires (in summer and autumn with higher smoke $PM_{2.5}$ concentrations in autumn) which presented different spatial distributions (summer: higher $PM_{2.5}$ concentrations in the northeastern to mid sub-region; autumn: higher $PM_{2.5}$ concentrations in the mid-eastern sub-region). The spatial distribution of average ensemble predicted $PM_{2.5}$ during these two wildfire weeks closely matched that of HYSPLIT-generated wildfire smoke $PM_{2.5}$ (Fig. 8-c vs. Fig. 9-a; Fig. 8-e vs. Fig. 9-b). Also, see Supplementary Fig. S15 and S16 for the comparison between total predicted $PM_{2.5}$ and wildfire smoke $PM_{2.5}$ (HYSPLIT) for the weeks before and after the wildfire weeks. We observed similar patterns during wildfire impacted weeks in other years. We also compared the time series of observed (at smoke impacted sites), ensemble model predicted and HYSPLIT-derived $PM_{2.5}$ for these two wildfire weeks and found that our model was able to sufficiently capture the $PM_{2.5}$ temporal peaks caused by wildfires (Supplementary Fig. S17 and S18). These results demonstrated that our method can capture spatial distribution and temporal peaks of $PM_{2.5}$ during wildfire smoke events.

5. Discussion

Spatiotemporal prediction of $PM_{2.5}$ over a large heterogeneous region such as California with high variability in emission sources, land-use, topography, meteorology and population is challenging. Using multisource data integrated into an ensemble deep learning framework

we were able to capture temporal and spatial trends over the region, including weeks where wildfires were present. As far as we know, this study is one of the first to leverage a variety of big data sources including M2GMI variables and wildfire smoke $PM_{2.5}$, and to use a residual deep learning to account for variability and improve estimation of $PM_{2.5}$ in California. Comparatively, in a statewide mixed model (Lee et al. 2016) and two recent national models (Di et al. 2016; Hu et al. 2017), California obtained R^2 of 0.66 to 0.80 (RMSE: 2.85–5.69 μg/m^3), lower than that of the eastern states of US. Our California-specific models generally had improved performance with greater R^2 (>7%) and lower RMSE (0.55–3.39 μg/m^3).

Particular matter (PM) contains both primary PM directly emitted into the air and secondary PM formed in the air by chemical reactions and other mechanisms from precursors emitted by fuel combustion and other sources (EPA 2014). Regarding composition, fine particles are made up of multiple chemical components, including carbon, sulfate and nitrate compounds as well as crustal materials (e.g., soil, dust and ash). California has a mixture of major urban areas with dense traffic network and industrial facilities, rural areas with agriculture, deserts and intensive smoke events (e.g., wildfires), which results in multiple emission sources and complexity in constituents for $PM_{2.5}$. In addition to observed and imputed MAIAC AOD (Li et al. 2020), we used traffic and/or land-use variables to account for the emission influence, as done in many studies (Beckerman et al. 2013; Di et al. 2019; Hu et al. 2017; Huang et al. 2018; Zhai et al. 2018). But land-use variables lack temporal variation and only indirectly reflect the emission influence, thus making limited contribution to estimation of $PM_{2.5}$. Several variables from the M2GMI dataset, not normally used in previous studies, made important contributions to explain the variability of $PM_{2.5}$, as measured by the SHAP values. Carbon monoxide concentrations and O_3 dry deposition were important predictors presumably because they broadly indicated the location and intensity of primary combustion sources and correlated with secondary formation of particles, respectively. Sea salt aerosol concentrations contributed perhaps because they distinguished coastal and inland aerosol characteristics. These variables were included along with variables like $PM_{2.5}$ black carbon concentrations which were strongly suspected of explaining $PM_{2.5}$ variability. Different from the MAIAC AOD, traffic and land-use variables, these M2GMI variables compensated the insufficiency in the data of emissions and constituents of $PM_{2.5}$ for California and can be used as important predictors for estimation of $PM_{2.5}$.

Meteorology also plays an important role in the formation and variability of particle matter (Tai et al. 2010). For example, air temperature, sunlight, water vapor and humidity can affect shifting between solid/liquid and gaseous phases; wind can transport fine particle over long distances; and planetary boundary layer (PBL) can play an important role in the turbulent mixing and vertical distribution of pollutants in the lower troposphere (Wang et al. 2019). The PBL height determines the volume available for pollution dispersion and transport, and significantly affects vertical structure and turbulent mixing that is responsible for variability of ground air quality. Undoubtedly, as a key input, PBLH is a critical variable that influences ground concentration of air pollutants including $PM_{2.5}$ (Knote et al. 2015; Su et al. 2018). In our study, the gridMET dataset provided high-resolution meteorological parameters (air temperature, wind speed, humidity, shortwave radiation and precipitation) but lacked other important parameters such as PBLH and wind speed at different altitudes. Therefore, we

extracted the PBLH variable from M2GMI that was critically used in the conversion of column satellite AOD to ground aerosol extinction coefficient (improving the correlation between AOD and $PM_{2.5}$ by 0.22), and estimation of $PM_{2.5}$. In addition, we derived the indicator of stagnation and wind sheer/mechanical mixing from wind speeds at the altitudes of 2m, 10m and 50m. Wind sheer/mixing presented high correlation with $PM_{2.5}$ compared with many other features. This study shows the important roles of the critical meteorological parameters, especially vertical ones, and pollutant concentrations from the M2GMI dataset in spatiotemporal estimation of $PM_{2.5}$. The M2GMI dataset is available globally from 1980 to 2018 and can be effectively used to obtain important parameters for estimation of $PM_{2.5}$.

California has extensive wildfires each year that can result in peak $PM_{2.5}$ concentration of smoke well beyond the typical range concentrations otherwise observed. Variability in spread and intensity of wildfire plumes can result in variability of spatial distribution of $PM_{2.5}$ during the wildfire seasons (Thompson and Calkin 2011), as illustrated in the results. In this study, we incorporated wildfire smoke $PM_{2.5}$ as a predictive feature to account for influence of wildfire events. Wildfire smoke $PM_{2.5}$ was generated using a top down approach for emissions and then a bottom up approach for the HYSPLIT dispersion modeling, with coincident measurements of fire radiative power (FRP) and AOD of MODIS (Ichoku and Ellison 2014). The results show the consistency between our predicted $PM_{2.5}$ surfaces and smoke $PM_{2.5}$ during the wildfire seasons. Few studies used the wildfire-related smoke feature to account for the influence of wildfire events, as ours (Chu et al. 2016). For California, wildfires are an important factor for spatiotemporal variability of $PM_{2.5}$ and an important public health concern, and the direct inclusion of $PM_{2.5}$ wildfire smoke in our model supports the representation of peak $PM_{2.5}$ concentrations that can typically be missed by similar modeling approaches.

Given the big and heterogeneous data from multiple sources, we leveraged ensemble deep learning, i.e. bagging of the base residual deep network to model the complex non-linear associations and interactions among features and $PM_{2.5}$. Residual learning was used in our models to boost the learning and improve the generalization. The autoencoder-based full residual deep network was demonstrated to be robust in non-linear modeling and our spatiotemporal imputation of MAIAC AOD (Li et al. 2020), and also used in downscaling of the M2GMI variables at a coarse spatial resolution to the target resolution of 1×1 km^2 in this study. For spatiotemporal estimation of $PM_{2.5}$, sensitivity analysis (Supplementary Table S5) shows that the base residual deep network improved testing R^2 over GAM by 21% and over feed-forward neural network by 5%. Bootstrapping using stratification by a spatiotemporal factor (county id and month) to de-correlate the training samples was important for the improvement of the test performance of our method compared to a simple block bootstrap. In simple block bootstrapping, the samples in each block were interdependent, which resulted in poorer test performance. Further, bagging of 100 base residual deep networks improved the testing R^2 over a single base model by 5% on average. The regular feed-forward neural network has been commonly used in estimation of $PM_{2.5}$ (Di et al. 2019; Di et al. 2016; Feng et al. 2015). Our ensemble method also generated the coefficient of variation of ensemble predictions as an uncertainty metric to inform error evaluation in exposure and health studies. Compared with recent existing methods, our method improved R^2 for 2008–2017 estimation (with the coefficient of variation) of $PM_{2.5}$ by at least 7%,

which shows that our method well accounted for spatiotemporal variability of $PM_{2.5}$ for California with high variability of $PM_{2.5}$.

This study has several limitations. First, multisource data at different resolutions (e.g., M2GMI variables and MAIAC AOD) were fused to obtain estimation of $PM_{2.5}$ at the spatial resolution of 1 km. This inconsistency among spatial resolutions might introduce bias in estimation. We used the autoencoder-based residual deep network to downscale coarse-resolution images to fine-resolution ones with the features of elevation and coordinates to capture spatial variability. With high test accuracy in downscaling, we could reduce the bias. Second, the uncertainty analysis showed high uncertainty (the coefficient of variation) over the land-use of deciduous and mixed forests, and water body (e.g., lakes, rivers) for predicted $PM_{2.5}$. Since such predictions with high uncertainty made up a small proportion of all the pixel-level predictions in California and most subject locations for exposure estimation are likely located in more urbanized areas, away from the rural areas, we do not expect this pattern in uncertainties to introduce significant bias into the assessment of downstream population health effects. Third, our method generated weekly, not daily $PM_{2.5}$ at a spatial resolution of 1×1 km^2 to ultimately support epidemiological studies of pregnancy outcomes; however, we are encouraged by its performance and expect that it can be adapted and generalized to daily resolution.

6. Conclusion

This study presents an ensemble deep learning method to fuse multisource heterogeneous big data to estimate $PM_{2.5}$ over California, a large region with high variability in emissions, topography, meteorology, and wildfire events. To account for high spatiotemporal variability and complexity of $PM_{2.5}$ across California and across 10 years from 2008 to 2017, we imputed massive missing MAIAC AOD, extracted factors related with the emissions and constituents, included critical meteorological factors (e.g., PBLH and wind speeds at different altitudes) from M2GMI, fused wildfire smoke, and included traffic and land-use variables as well as temporal basis functions. Elevation and the coordinates were also used to account for spatial variability. In this study, the full autoencoder residual deep network was used in downscaling to reduce the bias by the difference in spatial resolutions from multiple sources of data, imputation of massive missing MAIAC AOD due to cloud, snow and high surface reflectance, and as base models in ensemble deep learning to model the non-linear associations and complex interactions among the variables. Compared with the existing models for the California region, our method improved test R^2 to 0.87 and reduced test RMSE to 2.29$\mu g/m^3$. Prediction uncertainty estimates were derived, which can inform error assessment and model development in downstream evaluation of exposure and health effects of $PM_{2.5}$. Regarding the multisource features and the non-linear modeling method of deep learning, this study has important implications for improving spatiotemporal $PM_{2.5}$ estimation over a large, heterogeneous region.

Supplementary Material

Refer to Web version on PubMed Central for supplementary material.

Acknowledgments

The study was supported by the Lifecourse Approach to Developmental Repercussions of Environmental Agents on Metabolic and Respiratory Health NIH ECHO grants (4UH3OD023287) and the Southern California Environmental Health Sciences Center (National Institute of Environmental Health Sciences' grant, P30ES007048). The authors gratefully thank Dr. Melanie Follette-Cook, Dr. Pawan Gupta and Dr. Bryan Duncan for training, guidance and insights on NASA data products and their application in health and air quality studies. The MERRA-2 GMI Replay simulation is supported by the NASA Modeling, Analysis and Prediction (MAP) program and the high-performance computing resources were provided by the NASA Center for Climate Simulation (NCCS). Dr. Ralph J. Delfino, Dr. Costas Sioutas and Dr. Sina Hasheminassab are greatly appreciated for their support with independent test data from the USC site. Finally, the authors gratefully acknowledge the support of NVIDIA Corporation with the donation of the Titan Xp GPUs used in this research.

REFERENCES

Abatzoglou TJ (2011). Development of gridded surface meteorological datafor ecological applications and modelling. International Journal of Climatology, 2011

Allen RW, Adar SD, Avol E, Cohen M, Curl CL, Larson T, Liu LJS, Sheppard L, & Kaufman JD (2012). Modeling the Residential Infiltration of Outdoor PM2.5 in the Multi-Ethnic Study of Atherosclerosis and Air Pollution (MESA Air). Environmental Health Perspectives, 120, 824–830 [PubMed: 22534026]

Atkinson R, Kang S, Anderson H, Mills I, & Walton H. (2014). Epidemiological time series studies of PM2. 5 and daily mortality and hospital admissions: a systematic review and meta-analysis. Thorax, 69, 660–665 [PubMed: 24706041]

Bai Y, Wu L, Qin K, Zhang Y, Shen Y, & Zhou Y. (2016). A Geographically and TemporallyWeighted Regression Model for Ground-Level PM2.5 Estimation from Satellite-Derived 500 m Resolution AOD. Remote Sensing, 8, 262

Beckerman BS, Jerrett M, Serre M, Martin RV, Lee SJ, van Donkelaar A, Ross Z, Su J, & Burnett RT (2013). A Hybrid Approach to Estimating National Scale Spatiotemporal Variability of PM2.5 in the Contiguous United States. Environ Sci Technol, 47, 7233–7241 [PubMed: 23701364]

Bhandari A. (2020). Feature Scaling for Machine Learning: Understanding the Difference Between Normalization vs. Standardization. In

Biancofiore F, Busilacchio M, Verdecchia M, Tomassetti B, Aruffo E, Bianco S, Di Tommaso S, Colangeli C, Rosatelli G, & Di Carlo P. (2017). Recursive neural network model for analysis and forecast of PM10 and PM2.5. Atmospheric Pollution Research, 8, 652–659

Brauer M, Freedman G, Frostad J, van Donkelaar A, Martin RV, Dentener F, van Dingenen R, Estep K, Amini H, Apte JS, Balakrishnan K, Barregard L, Broday D, Feigin V, Ghosh S, Hopke PK, Knibbs LD, Kokubo Y, Liu Y, Ma SF, Morawska L, Sangrador JLT, Shaddick G, Anderson HR, Vos T, Forouzanfar MH, Burnett RT, & Cohen A. (2016). Ambient Air Pollution Exposure Estimation for the Global Burden of Disease 2013. Environ Sci Technol, 50, 79–88 [PubMed: 26595236]

Brokamp C, Jandarov R, Rao MB, LeMasters G, & Ryan P. (2017). Exposure assessment models for elemental components of particulate matter in an urban environment: A comparison of regression and random forest approaches. Atmospheric Environment, 151, 1–11 [PubMed: 28959135]

Carlstein E. (1986). The use of subseries values for estimating the variance of a general statistic from a stationary sequence. Ann. Statist, 14, 1171–1179

Chicco D. (2017). Ten quick tips for machine learning in computational biology. Biodata Mining, 10

Chu YY, Liu YS, Li XY, Liu ZY, Lu HS, Lu YA, Mao ZF, Chen X, Li N, Ren M, Liu FF, Tian LQ, Zhu ZM, & Xiang H. (2016). A Review on Predicting Ground PM2.5 Concentration Using Satellite Aerosol Optical Depth. Atmosphere, 7

Dennison PE, Brewer SC, Arnold JD, & Moritz MA (2014). Large wildfire trends in the western United States, 1984–2011. Geophysical Research Letters, 41, 2928–2933

Di Q, Amini H, Shi LH, Kloog I, Silvern R, Kelly J, Sabath MB, Choirat C, Koutrakis P, Lyapustin A, Wang YJ, Mickley LJ, & Schwartz J. (2019). An ensemble-based model of PM2.5 concentration across the contiguous United States with high spatiotemporal resolution. Environment International, 130

Di Q, Kloog I, Koutrakis P, Lyapustin A, Wang Y, & Schwartz J. (2016). Assessing PM2.5 Exposures with High Spatiotemporal Resolution across the Continental United States. Environ Sci Technol, 50, 4712–4721 [PubMed: 27023334]

EPA (2014). Guidance for PM2.s Permit Modeling. In: UNITED STATES ENVIRONMENTAL PROTECTION AGENCY

EPA (2017). Health and Environmental Effects of Particulate Matter (PM). In

EPA (2018). 2014 National Emissions Inventory, version 2 Technical Support Document. In. U.S. Environmental Protection Agency

Ester M, Kriegel PH, Sander J, & Xu X. (1996). A Density-Based Algorithm for Discovering Clusters in Large Spatial Databases with Noise. In, KDD'96: Proceedings of the Second International Conference on Knowledge Discovery and Data Mining (pp. 226–231)

Fast JD, Allan J, Bahreini R, Craven J, Emmons L, Ferrare R, Hayes PL, Hodzic A, Holloway J, Hostetler C, Jimenez JL, Jonsson H, Liu S, Liu Y, Metcalf A, Middlebrook A, Nowak J, Pekour M, Perring A, Russell L, Sedlacek A, Seinfeld J, Setyan A, Shilling J, Shrivastava M, Springston S, Song C, Subramanian R, Taylor JW, Vinoj V, Yang Q, Zaveri RA, & Zhang Q. (2014). Modeling regional aerosol and aerosol precursor variability over California and its sensitivity to emissions and long-range transport during the 2010 CalNex and CARES campaigns. Atmospheric Chemistry and Physics, 14, 10013–10060

Feng X, Li Q, Zhu YJ, Hou JX, Jin LY, & Wang JJ (2015). Artificial neural networks forecasting of PM2.5 pollution using air mass trajectory based geographic model and wavelet transformation. Atmospheric Environment, 107, 118–128

Finkenstadt B, Held L, & Isham V. (2007). Statistical Methods for Spatio-Temporal Systems. New York: Chapman & Hall/CRC

Friedman JH (2001). Greedy function approximation: a gradient boosting machine. Annals of statistics, 1189–1232

Fruin S, Urman R, Lurmann F, McConnell R, Gauderman J, Rappaport E, Franklin M, Gilliland FD, Shafer M, Gorski P, & Avol E. (2014). Spatial variation in particulate matter components over a large urban area. Atmos. Environ, 83, 211–219

Fu PF, Guo XB, Cheung FMH, & Yung KKL (2019). The association between PM2.5 exposure and neurological disorders: A systematic review and meta-analysis. Science of the Total Environment, 655, 1240–1248

Girguis MS, Li LF, Lurmann F, Wu J, Urman R, Rappaport E, Breton C, Gilliland F, Stram D, & Habre R. (2019). Exposure measurement error in air pollution studies: A framework for assessing shared, multiplicative measurement error in ensemble learning estimates of nitrogen oxides. Environment International, 125, 97–106 [PubMed: 30711654]

Girguis MS, Li LF, Lurmann F, Wu J, Urman R, Rappaport E, Breton C, Gilliland F, Stram D, & Habre R. (2020). Exposure Measurement Error in Air Pollution Studies: The Impact of Shared, Multiplicative Measurement Error on Epidemiological Health Risk Estimates. Air Quality, Atmosphere and Health, accepted

Goldstein A, Kapelner A, Bleich J, & Pitkin E. (2015). Peeking inside the black box: Visualizing statistical learning with plots of individual conditional expectation. Journal of Computational and Graphical Statistics, 24, 44–65

Goodfellow I, Bengio Y, & Courville A. (2016). Deep Learning. MIT Press

Guo Y, Tang Q, Gong D, & Zhang Z. (2017). Estimating ground-level PM2.5 concentrations in Beijing using a satellite-based geographically and temporally weighted regression model. Remote Sensing of Environment, 198, 140–149

Gupta P, Christopher SA, Wang J, Gehrig R, Lee Y, & Kumar N. (2006). Satellite remote sensing of particulate matter and air quality assessment over global cities. Atmospheric Environment, 40, 5880–5892

He KM, Zhang XY, Ren SQ, & Sun J. (2016a). Deep Residual Learning for Image Recognition. 2016 IEEE Conference on Computer Vision and Pattern Recognition (Cvpr), 770–778

He KM, Zhang XY, Ren SQ, & Sun J. (2016b). Identity Mappings in Deep Residual Networks. Computer Vision - Eccv 2016, Pt Iv, 9908, 630–645

Hu X, Belle JH, Meng X, Wildani A, Waller LA, Strickland MJ, & Liu Y. (2017). Estimating PM2.5 Concentrations in the Conterminous United States Using the Random Forest Approach. Environ Sci Technol, 51, 6936–6944 [PubMed: 28534414]

Hu XF, Waller LA, Lyapustin A, Wang YJ, Al-Hamdan MZ, Crosson WL, Estes MG, Estes SM, Quattrochi DA, Puttaswamy SJ, & Liu Y. (2014). Estimating ground-level PM2.5 concentrations in the Southeastern United States using MAIAC AOD retrievals and a two-stage model. Remote Sensing of Environment, 140, 220–232

Huang KY, Xiao QY, Meng X, Geng GN, Wang YJ, Lyapustin A, Gu DF, & Liu Y. (2018). Predicting monthly high-resolution PM2.5 concentrations with random forest model in the North China Plain. Environmental pollution, 242, 675–683 [PubMed: 30025341]

Ichoku C, & Ellison L. (2014). Global top-down smoke-aerosol emissions estimation using satellite fire radiative power measurements. Atmospheric Chemistry and Physics, 14, 6643–6667

Just AC, Wright RO, Schwartz J, Coull BA, Baccarelli AA, Tellez-Rojo MM, Moody E, Wang Y, Lyapustin A, & Kloog I. (2015). Using high-resolution satellite aerosol optical depth to estimate daily PM2. 5 geographical distribution in Mexico City. Environmental Science and Technology, 49, 8576–8584 [PubMed: 26061488]

Kloog I. (2016). Fine particulate matter (PM2.5) association with peripheral artery disease admissions in northeastern United States Int. J. Environ. Health Res, 26, 572–577 [PubMed: 27666297]

Kloog I, Koutrakis P, Coull BA, Lee HJ, & Schwartz J. (2011). Assessing temporally and spatially resolved PM2.5 exposures for epidemiological studies using satellite aerosol optical depth measurements. Atmospheric Environment, 45, 6267–6275

Knote C, Tuccella P, Curci G, Emmons L, Orlando JJ, Madronich S, Baro R, Jimenez-Guerrero P, Luecken D, Hogrefe C, Forkel R, Werhahn J, Hirtl M, Perez JL, San Jose R, Giordano L, Brunner D, Yahya K, & Zhang Y. (2015). Influence of the choice of gas-phase mechanism on predictions of key gaseous pollutants during the AQMEII phase-2 intercomparison. Atmospheric Environment, 115, 553–568

Koelemeijer RBA, Homan CD, & Matthijsen J. (2006). Comparison of spatial and temporal variations of aerosol optical thickness and particulate matter over Europe. Atmospheric Environment, 40, 5304–5315

Kunzli N, Jerrett M, Garcia-Esteban R, Basagana X, Beckermann B, Gilliland F, Medina M, Peters J, Hodis HN, & Mack WJ (2010). Ambient Air Pollution and the Progression of Atherosclerosis in Adults. PLoS One, 5

Larsen A, Yang S, Reich BJ, & Rappold AG (2020). A spatial causal analysis of wildland fire-contributed PM2. 5 using numerical model output. arXiv preprint arXiv:2003.06037

Larsen AE, Reich BJ, Ruminski M, & Rappold AG (2018). Impacts of fire smoke plumes on regional air quality, 2006–2013. Journal of Exposure Science and Environmental Epidemiology, 28, 319–327 [PubMed: 29288254]

Lee HJ (2019). Benefits of High Resolution PM2.5 Prediction using Satellite MAIAC AOD and Land Use Regression for Exposure Assessment: California Examples. Environ Sci Technol, 53, 12774–12783 [PubMed: 31566957]

Lee HJ, Chatfield RB, & Strawa AW (2016). Enhancing the Applicability of Satellite Remote Sensing for PM2.5 Estimation Using MODIS Deep Blue AOD and Land Use Regression in California, United States. Environ Sci Technol, 50, 6546–6555 [PubMed: 27218887]

Lee HK, Li Z, Kim JW, & Kokhanovsky A. (2009). Atmospheric Aerosol Monitoring from Satellite Observations: A History of Three Decades In Kim Y, Platt U, Gu MB, & Iwahashi H (Eds.), Atmospheric and Biological Environmental Monitoring,: Springer

Lee M, Kloog I, Chudnovsky A, Lyapustin A, Wang Y, Melly S, Coull B, Koutrakis P, & Schwartz J. (2015). Spatiotemporal prediction of fine particulate matter using high-resolution satellite images in the southeastern U.S. 2003–2011 J. Expo. Sci. Environ. Epidemiol., 26, 377–384 [PubMed: 26082149]

Li J, Carlson EB, & Lacis AA (2015). How well do satellite AOD observations represent the spatial and temporal variability of PM2.5 concentration for the United States? Atmos Environ, 102, 260–273

Li L, Franklin M, Girguis M, Lurmann F, Wu J, Pavlovic N, Breton C, Gilliland F, & Habre R. (2020). Spatiotemporal imputation of MAIAC AOD using deep learning with downscaling. Remote Sensing of Environment, 237, 111584 [PubMed: 32158056]

Li L, Zhang J, Meng X, Fang Y, Ge Y, Wang J, Wang C, Wu J, & Kan H. (2018). Estimation of PM2. 5 concentrations at a high spatiotemporal resolution using constrained mixed-effect bagging models with MAIAC aerosol optical depth. Remote Sensing of Environment, 217, 573–586

Li LF, Girguis M, Lurmann F, Wu J, Urman R, Rappaport E, Ritz B, Franklin M, Breton C, Gilliland F, & Habre R. (2019). Cluster-based bagging of constrained mixed-effects models for high spatiotemporal resolution nitrogen oxides prediction over large regions. Environment International, 128, 310–323 [PubMed: 31078000]

Liang RJ, Zhang B, Zhao XY, Ruan YP, Lian H, & Fan ZJ (2014). Effect of exposure to PM2.5 on blood pressure: a systematic review and meta-analysis. Journal of Hypertension, 32, 2130–2141 [PubMed: 25250520]

Lippmann M. (2014). Toxicological and epidemiological studies of cardiovascular effects of ambient air fine particulate matter (PM2.5) and its chemical components: Coherence and public health implications. Critical Reviews in Toxicology, 44, 299–347 [PubMed: 24494826]

Liu Y, Paciorek CJ, & Koutrakis P. (2009). Estimating Regional Spatial and Temporal Variability of PM2.5 Concentrations Using Satellite Data, Meteorology, and Land Use Information. Environmental Health Perspectives, 117, 886–892 [PubMed: 19590678]

Livingston JM, Redemann J, Shinozuka Y, Johnson R, Russell PB, Zhang Q, Mattoo S, Remer L, Levy R, Munchak L, & Ramachandran S. (2014). Comparison of MODIS 3 km and 10 km resolution aerosol optical depth retrievals over land with airborne sunphotometer measurements during ARCTAS summer 2008. Atmospheric Chemistry and Physics, 14, 2015–2038

Lu F, Xu D, Cheng Y, Dong S, Guo C, Jiang X, & Zheng X. (2015). Systematic review and meta-analysis of the adverse health effects of ambient PM2. 5 and PM10 pollution in the Chinese population. Environmental research, 136, 196–204 [PubMed: 25460637]

Lundberg SM, & Lee S-I (2017). A unified approach to interpreting model predictions. In, Advances in neural information processing systems (pp. 4765–4774)

Lv B, Hu Y, Chang HH, Russell AG, & Bai Y. (2016). Improving the accuracy of daily PM2.5 distributions derived from the fusion of ground-level measurements with aerosol optical depth observations, a case study in north China. . Environ Sci Technol, 50, 4752–4759 [PubMed: 27043852]

Lyapustin A, Korkin S, Wang Y, Quayle B, & Laszlo I. (2012). Discrimination of biomass burning smoke and clouds in MAIAC algorithm. Atmospheric Chemistry and Physics, 12, 9679–9686

Lyapustin A, Wang Y, Laszlo I, Kahn R, Korkin S, Remer L, Levy R, & Reid JS (2011). Multiangle implementation of atmospheric correction (MAIAC): 2. Aerosol algorithm. Journal of Geophysical Research-Atmospheres, 116

Lyapustin A, Wang YJ, Korkin S, & Huang D. (2018). MODIS Collection 6 MAIAC algorithm. Atmospheric Measurement Techniques, 11, 5741–5765

Monn C. (2001). Exposure assessment of air pollutants: a review on spatial heterogeneity and indoor/outdoor/personal exposure to suspended particulate matter, nitrogen dioxide and ozone. Atmospheric Environment, 35, 1–32

NASA (2018). MERRA-2 GMI In

NIST/SEMATECH (2016). e-Handbook of Statistical Methods.

Randles CA, da Silva AM, Buchard V, Colarco PR, Darmenov A, Govindaraju R, Smirnov A, Holben B, Ferrare R, Hair J, Shinozuka Y, & Flynn CJ (2017). The MERRA-2 Aerosol Reanalysis, 1980 Onward. Part I: System Description and Data Assimilation Evaluation. Journal of Climate, 30, 6823–6850 [PubMed: 29576684]

Reid CE, Brauer M, Johnston FH, Jerrett M, Balmes JR, & Elliott CT (2016). Critical Review of Health Impacts of Wildfire Smoke Exposure. Environmental Health Perspectives, 124, 1334–1343 [PubMed: 27082891]

Shirmohammadi F, Hasheminassab S, Saffari A, Schauer JJ, Delfino RJ, & Sioutas C. (2016). Fine and ultrafine particulate organic carbon in the Los Angeles basin: Trends in sources and composition. Science of the Total Environment, 541, 1083–1096

Stein AF, Draxler RR, Rolph GD, Stunder BJB, Cohen MD, & Ngan F. (2015). Noaa's Hysplit Atmospheric Transport and Dispersion Modeling System. Bulletin of the American Meteorological Society, 96, 2059–2077

Strode SA, Ziemke JR, Oman LD, Lamsal LN, Olsen MA, & Liu JH (2019). Global changes in the diurnal cycle of surface ozone. Atmospheric Environment, 199, 323–333

Su TN, Li ZQ, & Kahn R. (2018). Relationships between the planetary boundary layer height and surface pollutants derived from lidar observations over China: regional pattern and influencing factors. Atmospheric Chemistry and Physics, 18, 15921–15935

Tai AP, Mickley LJ, & Jacob DJ (2010). Correlations between fine particulate matter (PM2. 5) and meteorological variables in the United States: Implications for the sensitivity of PM2. 5 to climate change. Atmospheric Environment, 44, 3976–3984

Thompson MP, & Calkin DE (2011). Uncertainty and risk in wildland fire management: a review. Journal of environmental management, 92, 1895–1909 [PubMed: 21489684]

Thomson AM (2010). Neocortical layer 6, a review. Frontiers in Neuroanatomy, 4

Tolocka MP, Solomon PA, Mitchell W, Norris GA, Gemmill DB, Wiener RW, Vanderpool RW, Homolya JB, & Rice J. (2001). East versus West in the US: Chemical characteristics of PM2.5 during the winter of 1999. Aerosol Science and Technology, 34, 88–96

Toth TD, Zhang J, Campbell JR, Hyer EJ, Reid JS, Shi Y, & Westphal DL (2014). Impact of data quality and surface-to-column representativeness on the PM2.5/satellite AOD relationship for the contiguous United States. Atmospheric Chemistry and Physics, 14, 6049–6062

van Donkelaar A, Martin RV, & Park RJ (2006). Estimating ground-level PM2.5 using aerosol optical depth determined from satellite remote sensing. Journal of Geophysical Research-Atmospheres, 111

Wang C, Jia M, Xia H, Wu Y, Wei T, Shang X, Yang C, Xue X, & Dou X. (2019). Relationship analysis of PM 2.5 and boundary layer height using an aerosol and turbulence detection lidar. Atmospheric Measurement Techniques, 12, 3303–3315

Wang ZF, Chen LF, Tao JH, Zhang Y, & Su L. (2010). Satellite-based estimation of regional particulate matter (PM) in Beijing using vertical-and-RH correcting method. Remote Sensing of Environment, 114, 50–63

Wei J, Huang W, Li ZQ, Xue WH, Peng YR, Sun L, & Cribb M. (2019). Estimating 1-km-resolution PM2.5 concentrations across China using the space-time random forest approach. Remote Sensing of Environment, 231

Western Regional Air Partnership (2005). 2002 Fire Emission Inventory for the WRAP Region – Phase II, Project No. 178–6. In (pp. 1–97)

WHO (2013a). Health Effects of Particular Matter: Policy implications for countries in eastern Europe, Caucasus and central Asia. In

WHO (2013b). Review of evidence on health aspects of air pollution—REVIHAAP project: Final technical report. In. Bonn, Switzerland: The WHO European Centre for Environment and Health

Xiao Q, Wang Y, Chang HH, Meng X, Geng G, Lyapustin A, & Liu Y. (2017). Full-coverage high-resolution daily PM2.5 estimation using MAIAC AOD in the Yangtze River Delta of China. Remote Sensing of Environment, 199, 437–446

Xie Y, Wang Y, Zhang K, Dong W, Lv B, & Bai Y. (2015). Daily Estimation of Ground-Level PM2.5 Concentrations over Beijing Using 3 km Resolution MODIS AOD. Environ Sci Technol, 49, 12280–12288 [PubMed: 26310776]

Xing YF, Xu YH, Shi MH, & Lian YX (2016). The impact of PM2.5 on the human respiratory system. Journal of Thoracic Disease, 8, E69–E74 [PubMed: 26904255]

Yang LM, Jin SM, Danielson P, Homer C, Gass L, Bender SM, Case A, Costello C, Dewitz J, Fry J, Funk M, Granneman B, Liknes GC, Rigge M, & Xian G. (2018). A new generation of the United States National Land Cover Database: Requirements, research priorities, design, and implementation strategies. ISPRS Journal of Photogrammetry and Remote Sensing, 146, 108–123

Yuan L, Zhang Y, Gao Y, & Tian Y. (2019). Maternal fine particulate matter (PM2.5) exposure and adverse birth outcomes: an updated systematic review based on cohort studies. Environmental Science and Pollution Research, 26, 13963–13983 [PubMed: 30891704]

Zhai L, Li S, Zou B, Sang HY, Fang X, & Xu S. (2018). An improved geographically weighted regression model for PM2.5 concentration estimation in large areas. Atmospheric Environment, 181, 145–154

Zheng XR, Wang X, Wang TT, Zhang HX, Wu HJ, Zhang C, Yu L, & Guan YJ (2019). Gestational Exposure to Particulate Matter 2.5 (PM2.5) Leads to Spatial Memory Dysfunction and Neurodevelopmental Impairment in Hippocampus of Mice Offspring. Frontiers in Neuroscience, 12

Zhu XX, Liu Y, Chen YY, Yao CJ, Che Z, & Cao JY (2015). Maternal exposure to fine particulate matter (PM2.5) and pregnancy outcomes: a meta-analysis. Environmental Science and Pollution Research, 22, 3383–3396 [PubMed: 25163563]

Zou H, & Hastie T. (2005). Regularization and variable selection via the elastic net (vol B 67, pg 301, 2005). Journal of the Royal Statistical Society Series B-Statistical Methodology, 67, 768–768

Highlights

- California has high variability in $PM_{2.5}$ sources, meteorology and topography
- We used ensemble deep learning with multisource big data to improve $PM_{2.5}$ estimates
- We reliably imputed missing satellite AOD and fused wildfire dispersion estimates
- Our model achieved high $PM_{2.5}$ prediction performance with uncertainty estimates

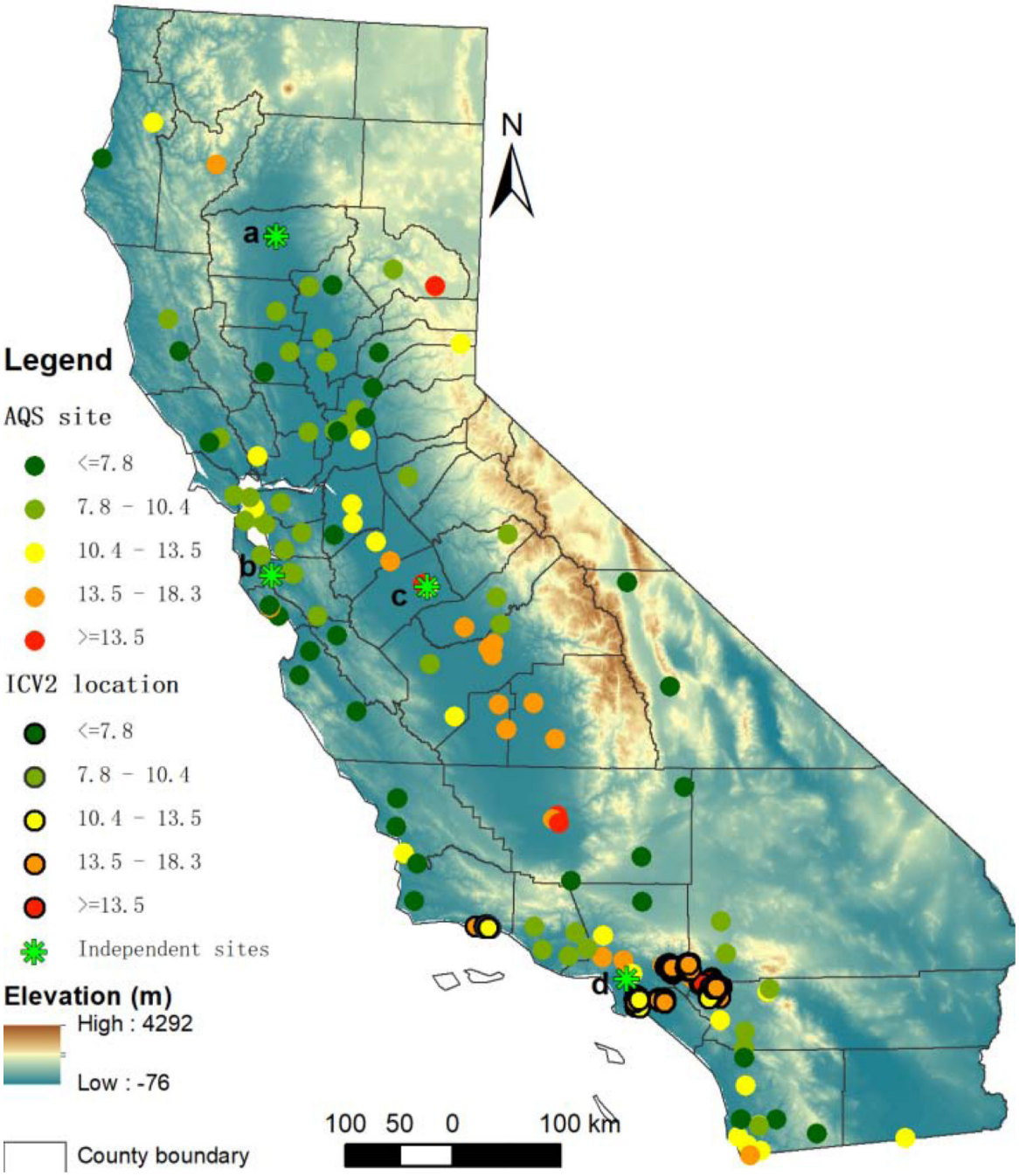

Fig 1.

California study region showing sampling period $PM_{2.5}$ averages at AQS and ICV2 monitoring sites and four independent test sites (a, b, c and d)

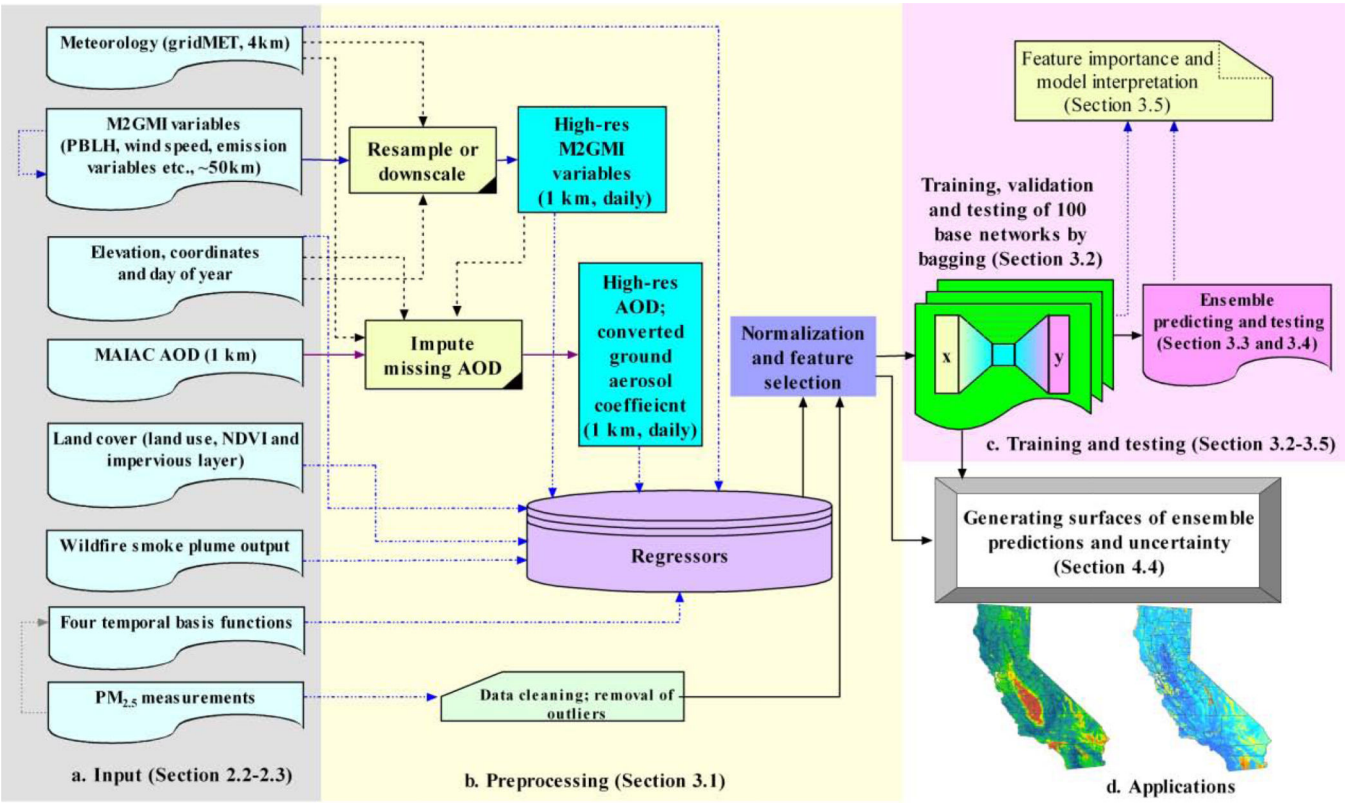

Fig 2.

Flowchart of the $PM_{2.5}$ modeling process in California

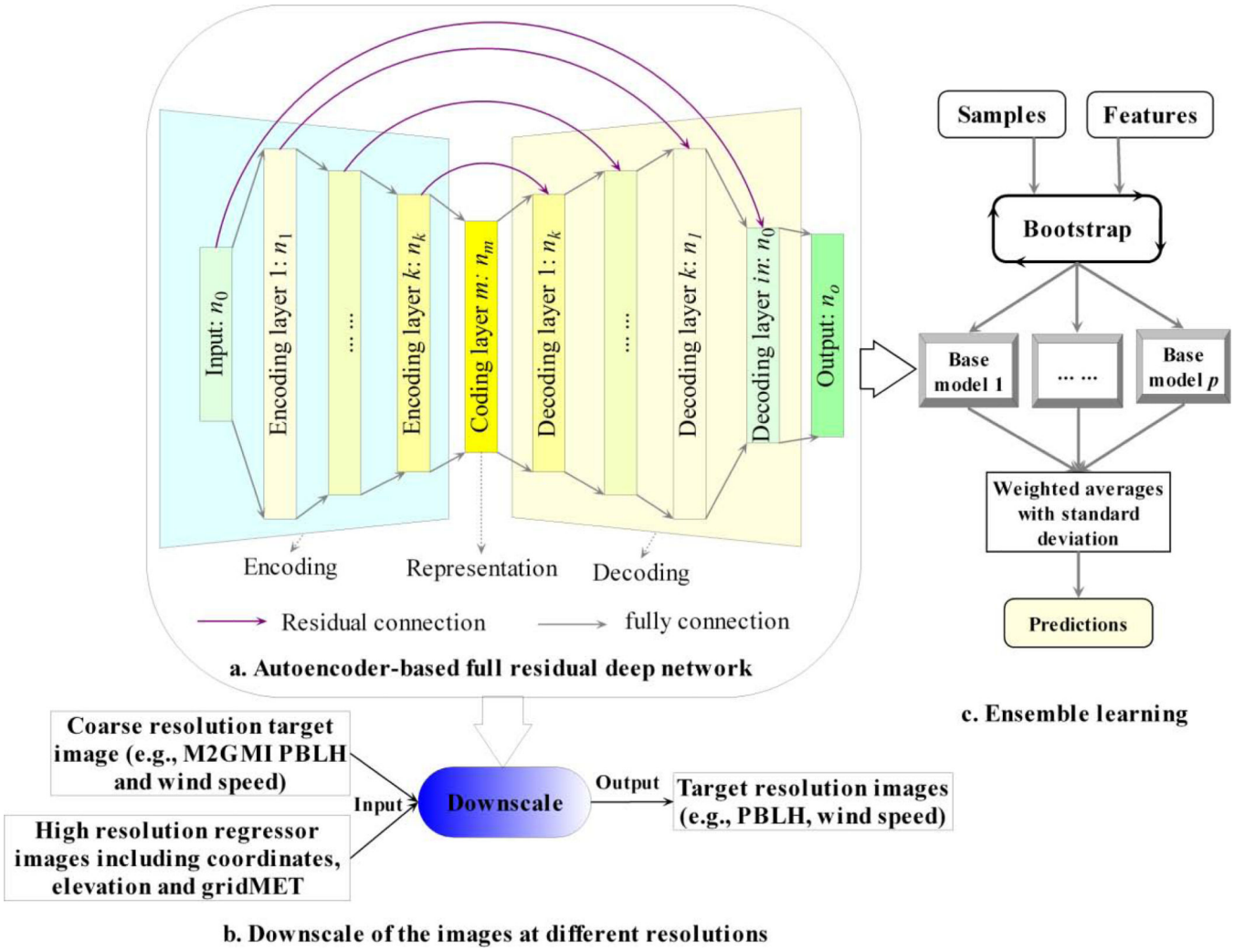

Fig. 3.

Autoencoder-based full residual deep network (a), downscaling (b) and ensemble learning (c).

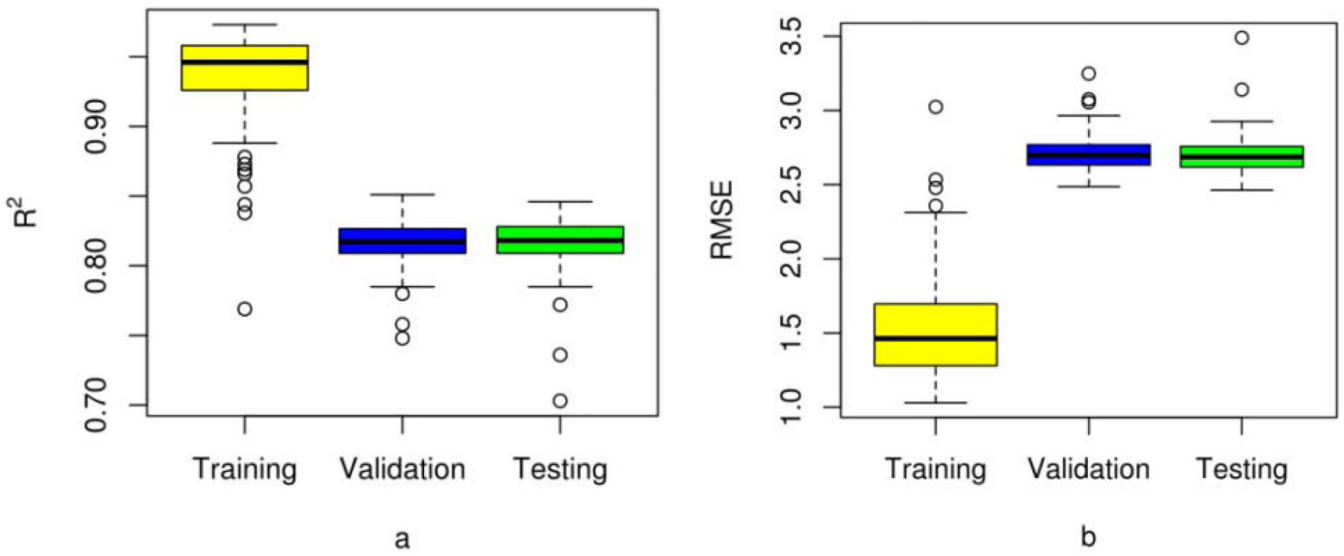

Fig. 4.
Boxplots of training, validation and testing R^2 (a) and RMSE in $\mu g/m^3$ (b).

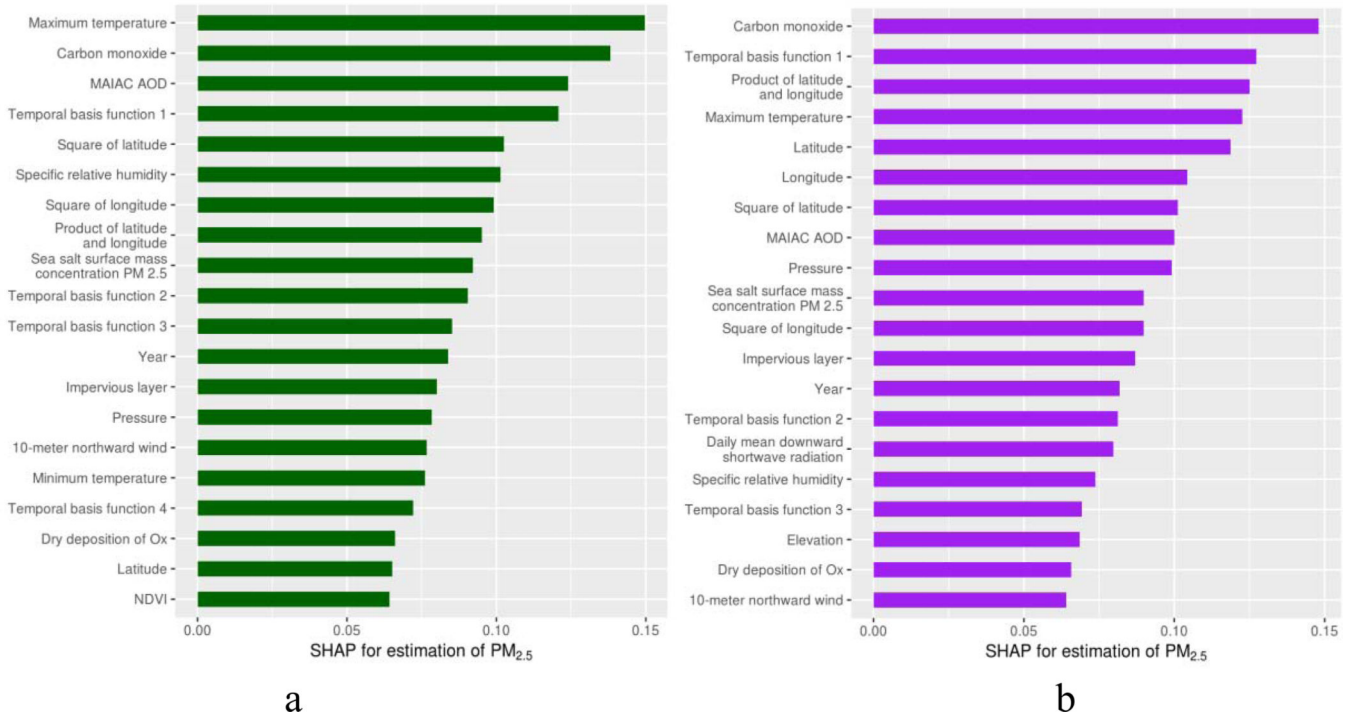

Fig. 5.

Bar plots of the feature importance of the top 20 features by SHAP (a. a single trained base model; b. averages of 100 trained models).

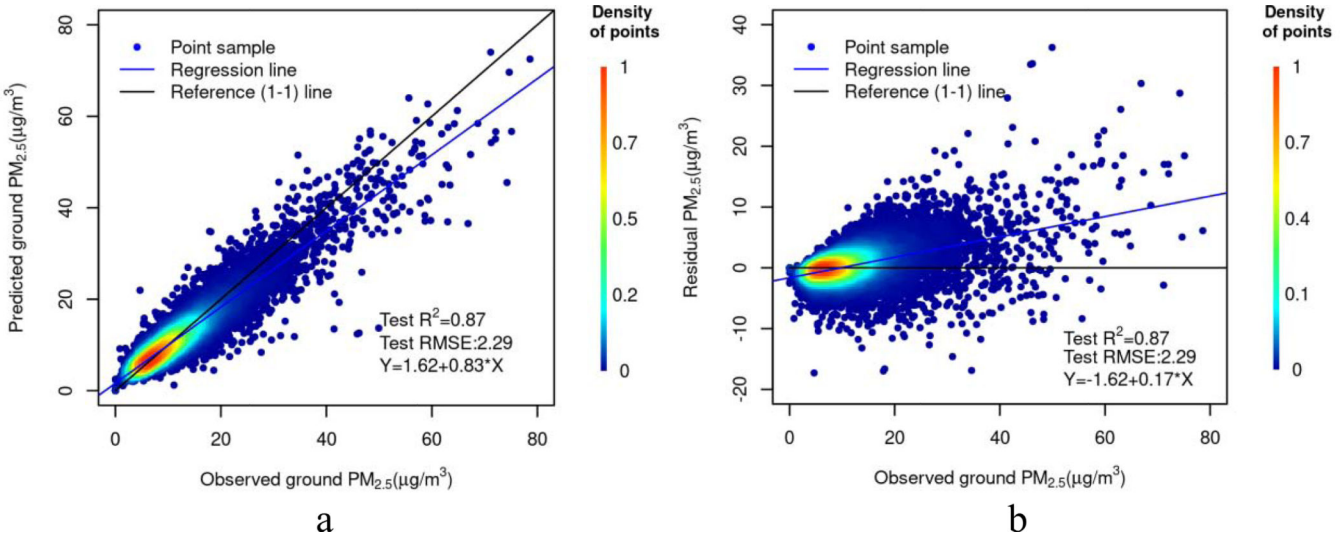

Fig. 6.

Scatter plots of observed vs. predicted $PM_{2.5}$ (a) and observed vs. residual $PM_{2.5}$ (b).

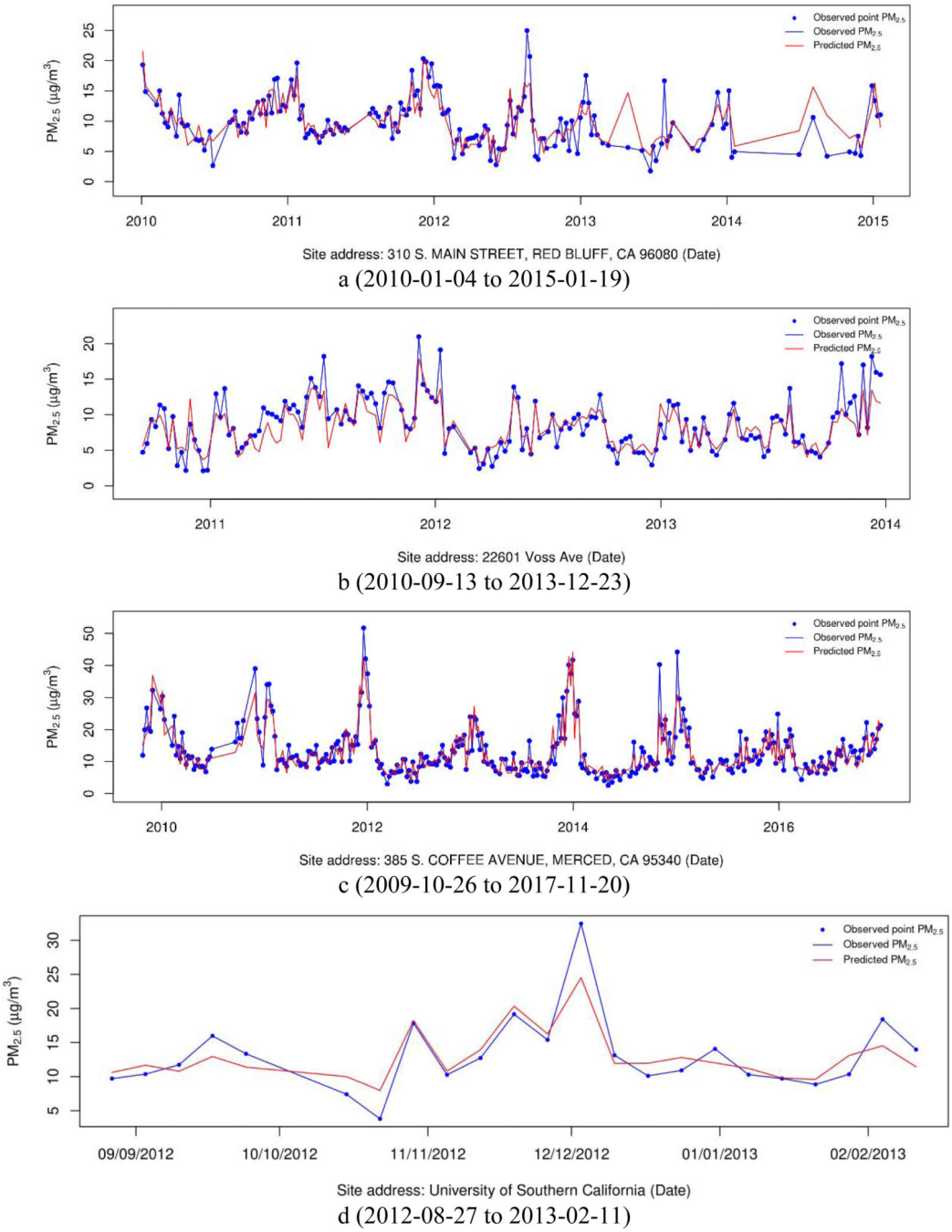

Fig. 7.

Time series of observed vs. predicted $PM_{2.5}$ in the independent test.

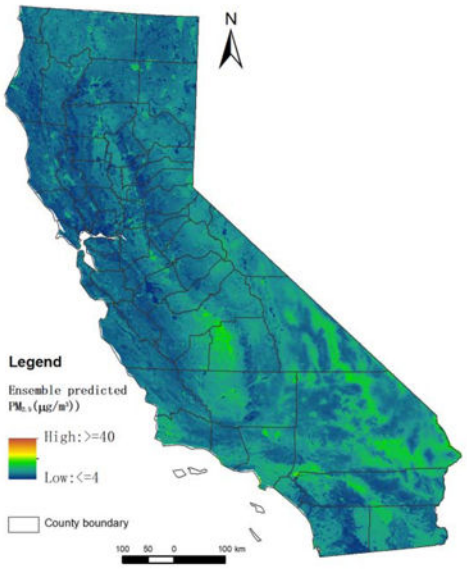

a. Ensemble predicted $PM_{2.5}$ for the spring week of 2008 (Apr. 21 to 27)

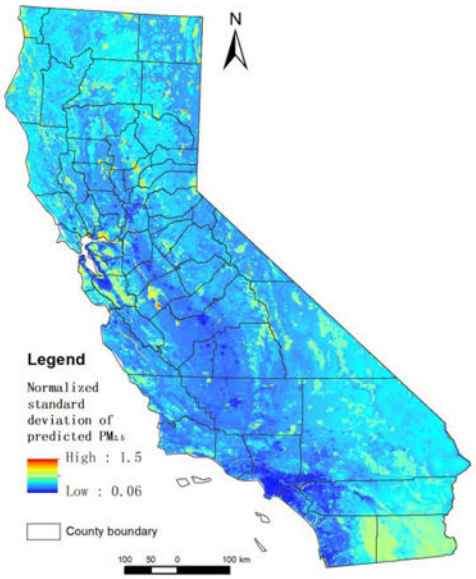

b. Coefficient of variation of ensemble predicted $PM_{2.5}$ for the spring week of 2008 (Apr. 21 to 27)

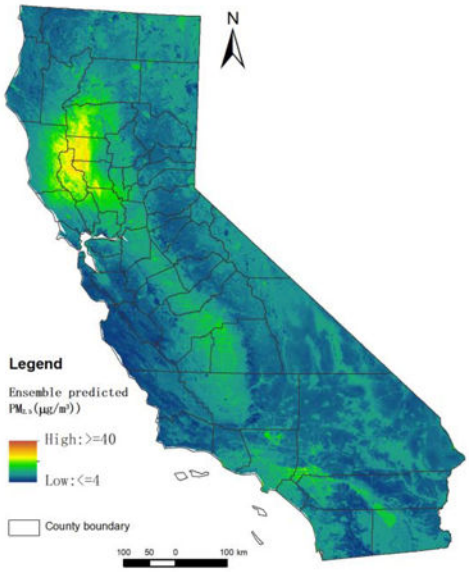

c. Ensemble predicted $PM_{2.5}$ for the summer week of 2012 (Jul. 16 to 22)

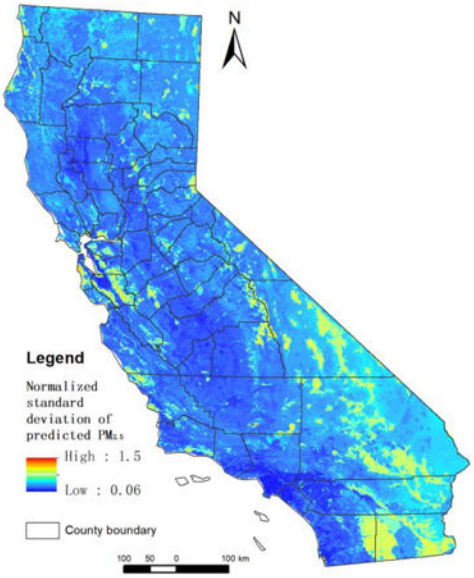

d. Coefficient of variation of ensemble predicted $PM_{2.5}$ for the week of 2012 (Jul. 16 to 22)

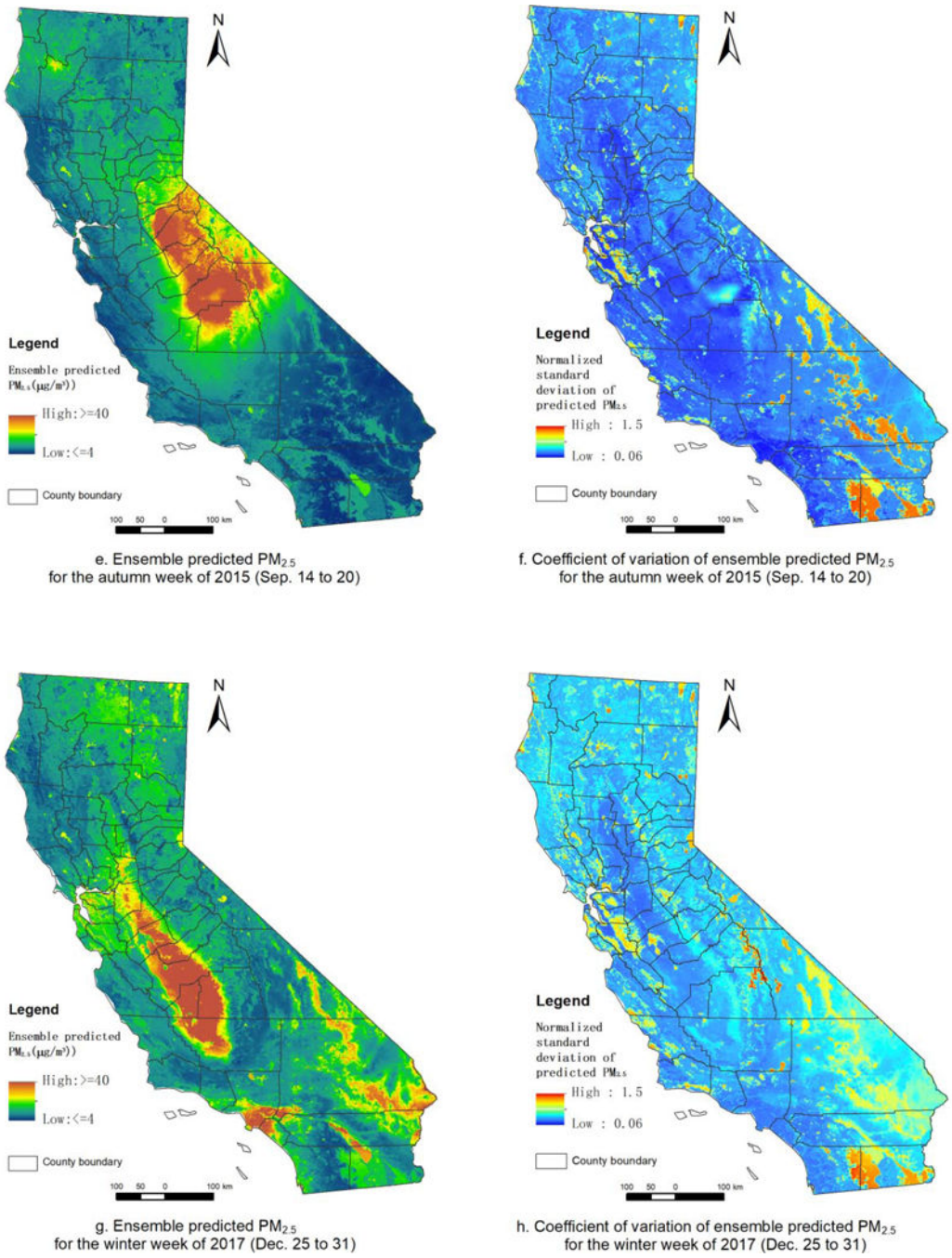

Fig. 8.

Surfaces of ensemble predicted $PM_{2.5}$ (a, c, e and g) and their the coefficient of variation (b, d, f and h) for four typical seasonal weeks in different years (a and b for spring week of 2008; c and d for summer week of 2015; e and f for autumn week of 2015; g and h for winter week of 2017).

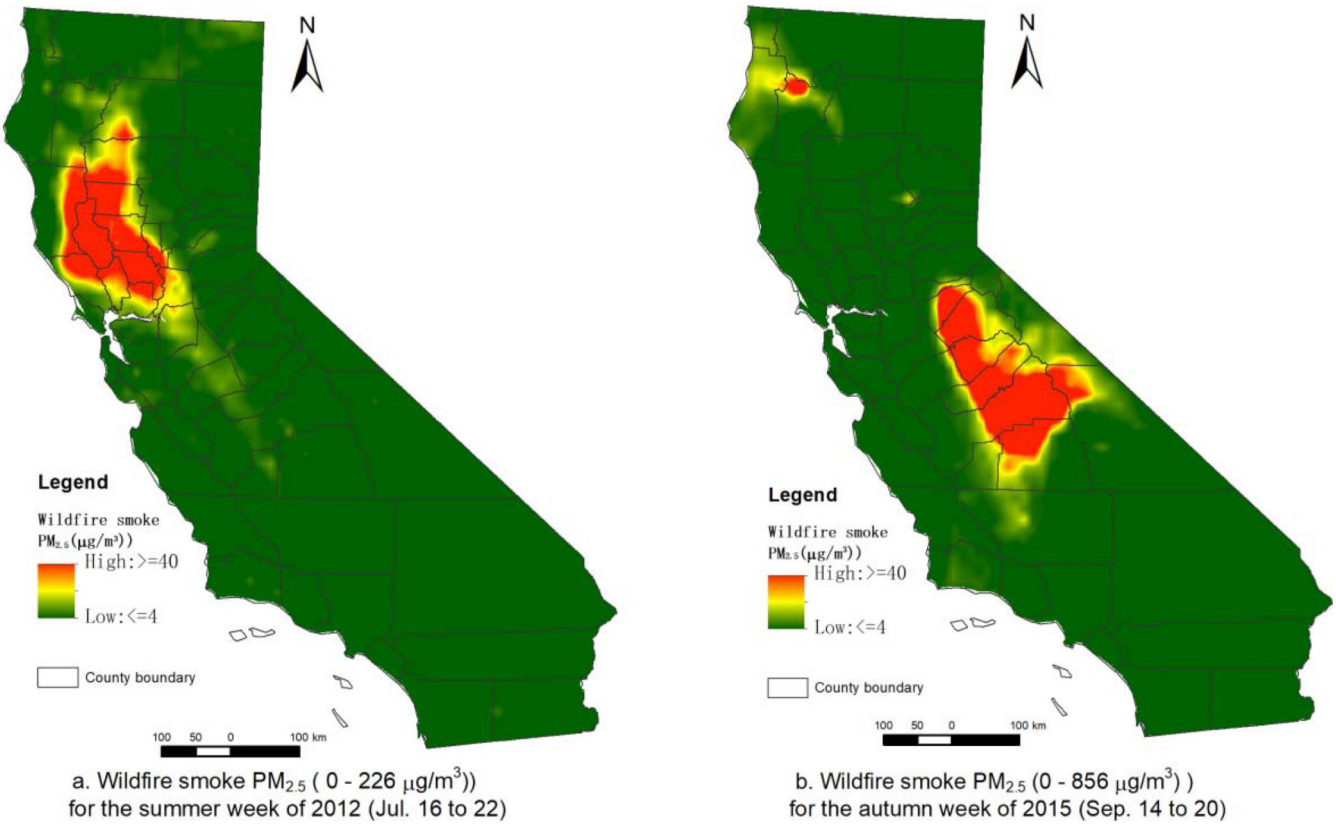

Fig. 9.

Distributions of HYSPLIT modeled wildfire smoke $PM_{2.5}$ for two wildfire season weeks in 2012 and 2015.

Table 1.

Summary of the predictive features with a high or moderate correlation with $PM_{2.5}$ concentration

Category	Name	Unit	Range	IQR	Mean	Median	Correlation
Satellite AOD	MAIAC AOD		0 to 1.55	0.05	0.07	0.06	0.47*
M2GMI or derived feature	Nitrate surface mass concentration-$PM_{2.5}$	kg/m^3	1.25E-13 to 5.13E-09	6.22E-10	5.28E-10	3.64E-10	0.37*
	Carbon monoxide	mol/mol	5.67E-08 to 9.27E-07	3.18E-08	1.17E-07	1.14E-07	0.35*
	Wind sheer/ mechanical mixing	m/s	0.08 to 2.46	0.43	0.9	0.88	−0.3*
	Dry deposition of O_x	$kg/m^2/s$	3.38E-11 to 2.84E-10	5.50E-11	1.30E-10	1.25E-10	−0.24*
	Sea salt surface mass concentration-$PM_{2.5}$	kg/m^3	3.38E-11 to 2.84E-10	2.35E-09	2.24E-09	1.72E-09	−0.2*
	SO_4 surface mass concentration	kg/m^3	5.32E-12 to 1.38E-08	9.33E-10	1.65E-09	1.39E-09	0.2*
	Black carbon surface mass concentration	kg/m^3	1.31E-10 to 6.97E-09	4.13E-10	6.59E-10	5.04E-10	0.2*
	Evaporation land	$Kg/m^2/s$	1.98E-11 to 5.04E-08	1.37E-05	1.15E-05	8.22E-06	−0.19*
	Indicator of stagnation	m/s	−0.48 to 2.7	0.63	0.7	0.72	−0.18*
	Mean planetary boundary layer height	m	121.58 to 3589.42	526.72	920.07	845.35	−0.12*
Meteorology	Wind speed	m/s	0.58 to 10.97	1.27	3.27	3.07	−0.33*
	Daily mean downward shortwave radiation	$watt/meter^2$	40.25 to 377.54	166.52	228.44	235.24	−0.14*
	Precipitation	mm/m^2	0 to 85.4	0.74	1.13	0	−0.12*
Temporal basis functions	Temporal basis function 1		−1.51 to 2.42	1.03	−0.22	−0.38	0.35*
	Temporal basis function 3		−1.23 to 2.39	1.01	0.79	0.85	−0.19*
Coordinates	Longitude	○	−124.2 to −115.48	3.46	−119.92	−120.1	0.18*
Remote sensing	Normalized difference vegetation index		723.8 to 7843.4	1465.3	3127.29	3073.6	−0.16*
	Impervious layer		0.03 to 87.79	43.74	41.29	44.34	0.15*
Land-use	Shrub/scrub		0 to 0.86	0.03	0.05	0	−0.14*
Wildfire	Wildfire smoke	$\mu g/m^3$	0 to 264.83	0.29	0.78	0.06	0.14*
Time index	Year		2008 to 2017	5	2013.33	2014	−0.15*

*: indicates statistical significance (*p-value*<0.01).

Table 2.

Performance statistics of 100 trained models in ensemble learning

	Training		Validation[a]		Testing[b]	
	Mean	**Range**	**Mean**	**Range**	**Mean**	**Range**
Sample size	17,629		4,407		12,776	
R^2 (range)	0.94	(0.77, 0.97)	0.82	(0.75, 0.85)	0.82	(0.70, 0.85)
RMSE ($\mu g/m^3$)	1.54	(1.03, 3.02)	2.70	(2.49, 3.24)	2.70	(2.46, 3.49)

[a]: the samples not used to train the models but used to validate the model (adjusting the hyper-parameters to get an optimal effect);

[b]: the samples used to test the trained models (not used in training and validation).

Table 3.

Performance of ensemble predictions in the independent test

	All samples	AQS samples	USC ICV2 samples
Sample size	12,776	12,266	510
R^2 (range)	0.87	0.87	0.82
RMSE ($\mu g/m^3$)	2.29	2.30	2.70

Table 4.

Performance for the time series in independent test

Site address	Source	#Time slices	Correlation	Mean $PM_{2.5}$ ($\mu g/m^3$)	R^2	RMSE ($\mu g/m^3$)
a. 310 S. Main St., Red Bluff, CA	AQS	171	0.82	9.88	0.67	2.36
b. 22601, Voss Av., Cupertino, CA	AQS	162	0.90	8.70	0.76	1.80
c. 385 S. Coffee Av., Merced, CA	AQS	329	0.93	13.32	0.87	2.81
d. University of Southern California	Shirmohammadi et al. (2016)	34	0.92	13.04	0.78	2.55